The Astrophysical Journal, 701:260–282, 2009 August 10 doi:10.1088/0004-637X/701/1/260
© 2009. The American Astronomical Society. All rights reserved. Printed in the U.S.A.

STRUCTURE AND EVOLUTION OF PRE-MAIN-SEQUENCE CIRCUMSTELLAR DISKS

Andrea Isella, John M. Carpenter, and Anneila I. Sargent
Department of Astronomy, California Institute of Technology, MC 249-17, Pasadena, CA 91125, USA; isella@astro.caltech.edu
Received 2009 February 16; accepted 2009 June 15; published 2009 July 21

ABSTRACT

We present new subarcsecond (∼0.″7) Combined Array for Research in Millimeter-wave Astronomy (CARMA) observations of the 1.3 mm continuum emission from circumstellar disks around 11 low- and intermediate-mass pre-main-sequence stars. High-resolution observations for three additional sources were obtained from the literature. In all cases the disk emission is spatially resolved. We adopt a self-consistent accretion disk model based on the similarity solution for the disk surface density and constrain the dust radial density distribution on spatial scales of about 40 AU. Disk surface densities appear to be correlated with the stellar ages where the characteristic disk radius increases from ∼20 AU to ∼100 AU over about 5 Myr. This disk expansion is accompanied by a decrease in the mass accretion rate, suggesting that our sample disks form an evolutionary sequence. Interpreting our results in terms of the temporal evolution of a viscous α-disk, we estimate (1) that at the beginning of the disk evolution about 60% of the circumstellar material was located inside radii of 25–40 AU, (2) that disks formed with masses from 0.05 to 0.4 $M_{\odot}$, and (3) that the viscous timescale at the disk initial radius is about 0.1–0.3 Myr. Viscous disk models tightly link the surface density $\Sigma(R)$ with the radial profile of the disk viscosity $\nu(R) \propto R^{\gamma}$. We find values of γ ranging from −0.8 to 0.8, suggesting that the viscosity dependence on the orbital radius can be very different in the observed disks. Adopting the α parameterization for the viscosity, we argue that α must decrease with the orbital radius and that it may vary between 0.5 and 10^{-4}. From the inferred disk initial radii we derive specific angular momenta, j, for parent cores of $(0.8-4)\times10^{-4}$ km s^{-1} pc. Comparison with the values of j in dense cores suggests that about 10% of core angular momentum and 30% of the core mass are conserved in the formation of the star/disk system. We demonstrate that the similarity solution for the surface density for $\gamma < 0$ can explain the properties of some "transitional disks" without requiring discontinuities in the disk surface density. In the case of LkCa 15, a smooth distribution of material from few stellar radii to about 240 AU can produce both the observed spectral energy distribution and the spatially resolved continuum emission at millimeter wavelengths. Finally we show that among the observed sample, TW Hya is the only object that has a disk radius comparable with the early solar nebula.

Key words: planetary systems: formation – planetary systems: protoplanetary disks – stars: pre-main sequence

Online-only material: color figure

1. INTRODUCTION

Spatially unresolved observations of the infrared and mm-wave emission from nearby pre-main-sequence stars surrounded by disks suggest that most of the circumstellar dust dissipates on timescales between 1 and 10 Myr (see, e.g., Hernández et al. 2007). Nevertheless, it remains very uncertain how disk evolution proceeds in individual systems and, in particular, whether all circumstellar disks give rise to planetary systems. Over the last ten years a large number of circumstellar disks in nearby star-forming regions have been observed using long baseline millimeter and submillimeter interferometers. These observations have spatially resolved the disk emission to infer the radial distribution of gas and dust. However, at the distance of the nearby star-forming regions (100–200 pc), the typical angular resolution of 1.″5–3″ (Rodmann et al. 2006; Andrews et al. 2007; Kitamura et al. 2002; Dutrey et al. 1996) could not constrain the detailed structure of disks, which typically have radii of only a few hundred AU.

Higher angular resolution mm-wave observations remain challenging and the number of disks observed at angular resolution higher than 1″ is still very small and essentially restricted to more massive and luminous pre-main-sequence circumstellar disks such as LkHα 330 (Brown et al. 2008), HD 163296 (Isella et al. 2007), AB Aur, MWC 480, DM Tau and LkCa 15 (Piétu et al. 2005, 2006, 2007), CQ Tau (Testi et al. 2003), DL Tau, UZ Tau, BP Tau and GM Aur (Simon et al. 2000), TW Hya (Wilner et al. 2000), and GG Tau (Guilloteau et al. 1999). Even for this small sample the radial distribution and kinematics of the circumstellar material vary considerably from object to object. Since the observed objects are characterized by stellar ages between ∼0.1 and ∼10 Myr, which is probably a considerable fraction of the disk life time, variations in the dust properties may also be representative of different evolutionary stages. Differences in disk structure are believed to result from variation in the total angular momenta, masses, chemical compositions, and magnetic fields, during the collapse of the parent molecular core (see, e.g., Hueso & Guillot 2005). Disk structure in multiple systems or in dense star-forming regions can also be influenced by the dynamical perturbation induced by close-by companions or by strong interstellar radiation field (see, e.g., Alexander et al. 2006). Detailed investigations of disk structure and of the origins of any observed difference are clearly necessary to improve our understanding of the formation of planetary systems.

Here we present subarcsecond observations of circumstellar disks around 14 nearby pre-main-sequence stars. New 1.3 mm continuum observations of 11 objects in the Taurus and Ophiuchus star-forming regions, CY Tau, DG Tau, DM Tau, DN Tau, DR Tau, GO Tau, LkCa15, RY Tau, UZ Tau E, GSS 39, SR 24 S,

Table 1
Sample Properties

Object (1)	α(2000) (2)	δ(2000) (3)	ST (4)	L_* (5)	T_* (6)	log(L_{acc}) (7)	Ref. (8)	R_* (9)	log($\dot{M}_{acc}$) (10)	M_* (11)	Age (12)
CY Tau	04:17:33.73	28:20:46.95	M1	0.47	3720	−1.34	1	1.68	−8.52	0.4	0.8
DG Tau	04:27:04.70	26:06:16.39	M0	1.70	3890	0.70	7	2.87	−6.39	0.3	0.1
DM Tau	04:33:48.73	18:10:09.96	M1	0.25	3720	−1.05	1	1.20	−8.32	0.5	3.0
DN Tau	04:35:27.37	24:14:58.90	M0	0.91	3850	−1.80	1	2.14	−8.97	0.4	0.5
DR Tau	04:47:06.22	16:58:42.87	K7	3.00	4060	0.44	3,6,7	3.19	−6.68	0.4	0.1
GO Tau	04:43:03.09	25:20:18.59	M0	0.28	3850	−0.98	1	1.23	−8.33	0.6	3.0
LkCa15	04:39:17.78	22:21:03.52	K5	0.74	4350	−1.75	1	1.60	−9.17	0.7	1.8
RY Tau	04:21:57.41	28:26:35.56	K1	7.60	5080	0.20	5	2.92	−7.11	2.0	0.5
UZ Tau E	04:32:43.07	25:52:31.14	M1	0.90	3720	0.17	5	2.28	−6.90	0.3	0.4
GM Aur	04:55:10.98	30:21:59.38	K7	0.74	4060	−1.15	1	1.4	−8.55	0.5	1.0
GSS 39	16:26:45.00	−24:23:07.70	M1	1.20	3720	−0.40	2	2.64	−7.43	0.3	0.1
SR 24 S	16:26:58.50	−24:45:36.90	K6	2.50	4170	0.03	2	3.03	−7.13	0.4	0.2
TW Hya	11:01:51.91	−34:42:17.02	K8	0.25	4000	−1.92	3	1.0	−9.38	0.7	7.0
MWC 275	17:56:21:29	−21:57:21.88	A1	36.0	9500	0.40	4	2.2	−7.12	2.3	5.0

Notes. In Column 5 we report the stellar luminosity in solar luminosities, in Column 6 the stellar temperature in K, in Column 7 the accretion luminosity in $L_\odot$/yr, in Column 9 the stellar radius in solar radii, in Column 10 the mass accretion rate in $M_\odot$/yr, in Column 11 the stellar mass in solar masses, and in Column 12 the stellar age in Myr.

References.(1) Hartmann et al. 1998; (2) Natta et al. 2006; (3) Muzerolle et al. 2000; (4) Garcia Lopez et al. 2006; (5) Kenyon & Hartmann 1995; (6) Calvet & Gullbring 1998; (7) Muzerolle et al. 1998.

were obtained with the Combined Array for Research in Millimeter Astronomy[1] (CARMA). For MWC 275 (HD163296), GM Aur, and TW Hya, we have reanalyzed published data from the SMA and Plateau de Bure interferometers (Hughes et al. 2008; Isella et al. 2007). For each object we derive the radial dust distribution by comparing the observed dust continuum emission with a self-consistent disk model based on the similarity solution for the surface density of a viscous Keplerian disk (Lynden-Bell & Pringle 1974).

In Section 2 we summarize the properties of the stellar sample. The interferometric observations and data reduction procedures are described in Section 3. In Section 4 we discuss the observations. Section 5 contains the description of the adopted disk model, while the results are presented in Section 6. The discussion and the conclusions follow in Sections 7 and 8.

2. THE SAMPLE

The 14 stars selected for study are listed in Table 1 together with the adopted luminosities, spectral types, temperatures, and accretion luminosities. All are nearby pre-main-sequence T Tauri stars with known 1.3 mm flux densities in excess of 50 mJy, to ensure high signal-to-noise ratios for the extended disk emission. Two targets, UZ Tau E and SR24 S, are members of multiple systems. The first nine objects of Table 1 are located in the Taurus-Auriga star-forming region, while GSS 39 and SR 24 S are in Ophiuchus. TW Hya is in the homonymous association, and MWC 275 (HD 163296) is an isolated Herbig Ae star. Based on observations of the molecular gas emission, the strong excess continuum emission at IR, mm, and radio wavelengths appears to originate from large amounts of gas and dust distributed in a rotating disk (Guilloteau et al. 1999; Dutrey et al. 1996; Simon et al. 2000; Qi et al. 2004; Isella et al. 2007).

2.1. Stellar Properties

For the objects in Taurus-Auriga and Ophiuchus we assume stellar distances of 140 ± 10 and 130 ± 15 pc, respectively (see Rebull et al. 2004). For TW Hya and MWC 275 we adopt the *Hipparcos* distances of 56 ± 5 pc (Wichmann et al. 1998) and 122 ± 20 pc (van den Ancker et al. 1998), respectively.

Stellar ages and masses are derived from the H–R diagram using theoretical tracks from D'Antona & Mazzitelli (1997, with the 1998 updated version available on the web; hereafter DM97) adopting published spectral types and luminosities (see Table 1). Assuming errors of about 30% in the stellar luminosity and half a spectral type in the spectral type classification, the resulting masses and ages are uncertain by 30%–50%. Although masses and ages are strongly dependent on the adopted stellar evolution model (Appendix A), the main results of the paper are almost independent of this choice, as discussed in Section 7.

Stellar radii based on the effective temperature and the bolometric luminosity were combined with the derived masses to provide mass accretion rates $\dot{M}_{acc}$, following the relation $\dot{M}_{acc} = L_{acc} R_*/(GM_*)$. Both quantities are listed in Table 1, together with stellar masses and ages.

3. OBSERVATIONS

Interferometric observations of the 11 disks in Table 2 were carried out with CARMA, which consists of six 10 m and nine 6 m antennas, and is located near Big Pine (CA) at an altitude of about 2200 m.

The data were obtained between 2007 October and 2008 April using the C and B array configurations to provide baseline lengths between 20 and 270 m and between 90 and 900 m, respectively, corresponding to angular resolutions of about 0.″7 and 0.″4 at 1.3 mm. The CARMA correlator was configured with two wide bands of 500 MHz each and one narrowband of 8 MHz centered at the frequency of 230.538 GHz, corresponding to the ^{12}CO (2–1) molecular transition. Only continuum emission observed in the wide 1 GHz band will be discussed here. Each source was observed for 4-8 hr to achieve a noise level between 1 and 5 mJy. Source names, array configurations, synthesized

[1] Support for CARMA construction was derived from the Gordon and Betty Moore Foundation, the Kenneth T. and Eileen L. Norris Foundation, the Associates of the California Institute of Technology, the states of California, Illinois, and Maryland,and the National Science Foundation. Ongoing CARMA development and operations are supported by the National Science Foundation under a cooperative agreement, and by the CARMA partner universities.

Table 2
Summary of CARMA Continuum Observations at 230 GHz

Object	Config.	Beam FWHM (″)	Beam P.A. (°)	Date	Phase Calibrators
CY Tau	C	1.05 × 0.72	77	2007 Nov 12	3C111, 3C123
DG Tau	C	0.87 × 0.78	−50	2007 Sep 30	3C111, 0530+135, 3C123
...	C	0.83 × 0.64	−72	2007 Oct 08	3C111, 0530+135, 3C123
...	B	0.43 × 0.27	−74	2007 Dec 14	3C111, 0530+135, 0510+180
DM Tau	C	0.82 × 0.60	−78	2007 Nov 05	3C111, 0530+135, 3C120
DN Tau	C	0.80 × 0.58	−76	2007 Nov 05	3C111, 0530+135, 3C120
DR Tau	C	0.92 × 0.76	−83	2007 Oct 09	3C111, 0530+135, 0449+113
...	C	0.84 × 0.70	82	2007 Oct 24	0530+135, 0449+113
...	B	0.46 × 0.34	39	2007 Feb 06	0530+135, 0449+113
GO Tau	C	0.87 × 0.65	88	2007 Nov 07	0530+135, 3C123
LkCa15	C	0.83 × 0.70	70	2007 Oct 27	3C111, 0530+135, 3C123
RY Tau	C	0.89 × 0.74	−61	2007 Oct 01	3C111, 3C123
...	C	1.14 × 0.60	−73	2007 Oct 22	3C111, 0530+135, 3C123
UZ Tau E[a]	C	0.82 × 0.69	79	2007 Oct 27	3C111, 0530+135, 3C123
GSS 39	C	1.42 × 0.85	−6	2008 Apr 12	1625-254, 1733-130
SR 24 S[b]	C	1.45 × 0.91	−6	2008 Apr 13	1625-254, 1733-130

Notes.
[a] UZTau W, the other component of the UZTau system, was detected at 4σ level with an integrated 1.3 mm flux of about 30 mJy (see Figure 1)
[b] The other component of the SR 24 binary system, SR 24 N (Patience et al. 2008), was not detected.

beam sizes, dates, and adopted gain calibrators are summarized in Table 2.

The data were reduced using the MIRIAD software package. The resulting 1.3 mm maps, obtained using natural weighting, are shown in Figure 1. Bandpass calibration relied on observations of 3C273 and absolute flux calibration was set by observing Uranus. Since we are interested in resolving the disk extended structures we took particular care in correcting for the atmospheric turbulence which may result in artificially extended sources. For each set of observations, we calibrated the data by observing every 15 minutes a bright unresolved calibrator located within 20° from the target. Fitting a bidimensional Gaussian profile to the calibrator image, we measured the seeing and corrected the data using the SEEING option of the UVCAL MIRIAD command. Residual effects of the seeing are then eliminated by rejecting the UV points on which the atmospheric turbulence introduces a flux loss higher than 10% on the phase calibrator. To check the quality of the phase calibration we observed, if available, a fainter second point source located within 5° from to the science target. We then verified that, after applying the calibration solution derived for the bright calibrator, we obtain an unresolved image of this second calibrator.

Details of the 1.3 mm SMA dust continuum observations and data calibration of GM Tau and TW Hya can be found in Hughes et al. (2008, and references therein). The angular resolution of these observations was about 1″ at 1.3 mm. Similarly, details on the PdB observations of MWC 275 can be found in Isella et al. (2007). In this case the resolution was 2″ × 0.″4. The 1.3 mm maps of these three sources are shown in Figure 2.

4. OBSERVATIONAL RESULTS

The observed continuum emission toward each of the disks is spatially resolved, centered on the position of the parent star and shows an almost centro-symmetric surface brightness profile. In Table 3 we report the spatially integrated flux (Column 2), the angular size obtained by fitting the continuum map with a bidimensional Gaussian profile (Column 3), a first-order derivation of the disk inclination measured from the aspect ratio of the Gaussian fitting (Column 4), and the position angle measured east from north (Column 5). Column 6 shows the disk radius, R_g, defined as the radius containing 95% of the observed emission. In practice, $R_g \sim 1.4 \times$ FWHM measured along the apparent disk major axis assuming the stellar distances discussed in Section 2. Given the sensitivity of the observations and the fact that the dust emission is optically thin, this radius provides only a rough estimate of the real extent of the disk.

Table 3
Properties of the 1.3 mm Dust Emission

Object	Flux (mJy)	Source size FWHM (″)	i (°)	P.A. (°)	R_g (AU)
CY Tau	117 ± 20	1.25 × 0.60	61	150	230
DG Tau	317 ± 28	0.52 × 0.46	28	11	95
DM Tau	90 ± 8	0.89 × 0.82	22	20	160
DN Tau	93 ± 8	0.68 × 0.53	39	86	125
DR Tau	109 ± 11	0.48 × 0.39	36	108	90
GO Tau	57 ± 8	0.86 × 0.69	37	107	160
LkCa15	119 ± 15	1.39 × 0.71	59	55	250
RY Tau	227 ± 20	0.63 × 0.38	53	23	115
UZ Tau E	126 ± 12	0.88 × 0.64	43	66	160
GM Aur	189 ± 15	1.38 × 1.08	45	106	270
GSS 39	282 ± 20	1.33 × 0.87	49	116	260
SR 24 S	197 ± 17	1.64 × 0.96	54	60	320
TW Hya	543 ± 45	1.06 × 1.04	12	89	76
MWC 275	705 ± 12	1.49 × 1.12	41	135	250

The measured integrated fluxes are in good agreement (20%) with earlier interferometric observations at lower angular resolution, suggesting that only a small fraction of the flux is emitted on completely resolved out disk scales. We therefore assume that the CARMA observations trace the bulk of the disk emission. Disk radii range from 90 AU (DR Tau) to 320 AU (SR 24 S) and the surface brightness slopes vary from steep (e.g., DG Tau, DR Tau, DN Tau) to quite shallow (e.g., RY Tau, CY Tau, LkCa 15, GSS 39). This latter point is illustrated in Figure 3, which shows the normalized visibility amplitude V as a function of the baseline length between 0 and 270 m for four disks. The most extended source, GSS 39 (filled circles), is completely resolved

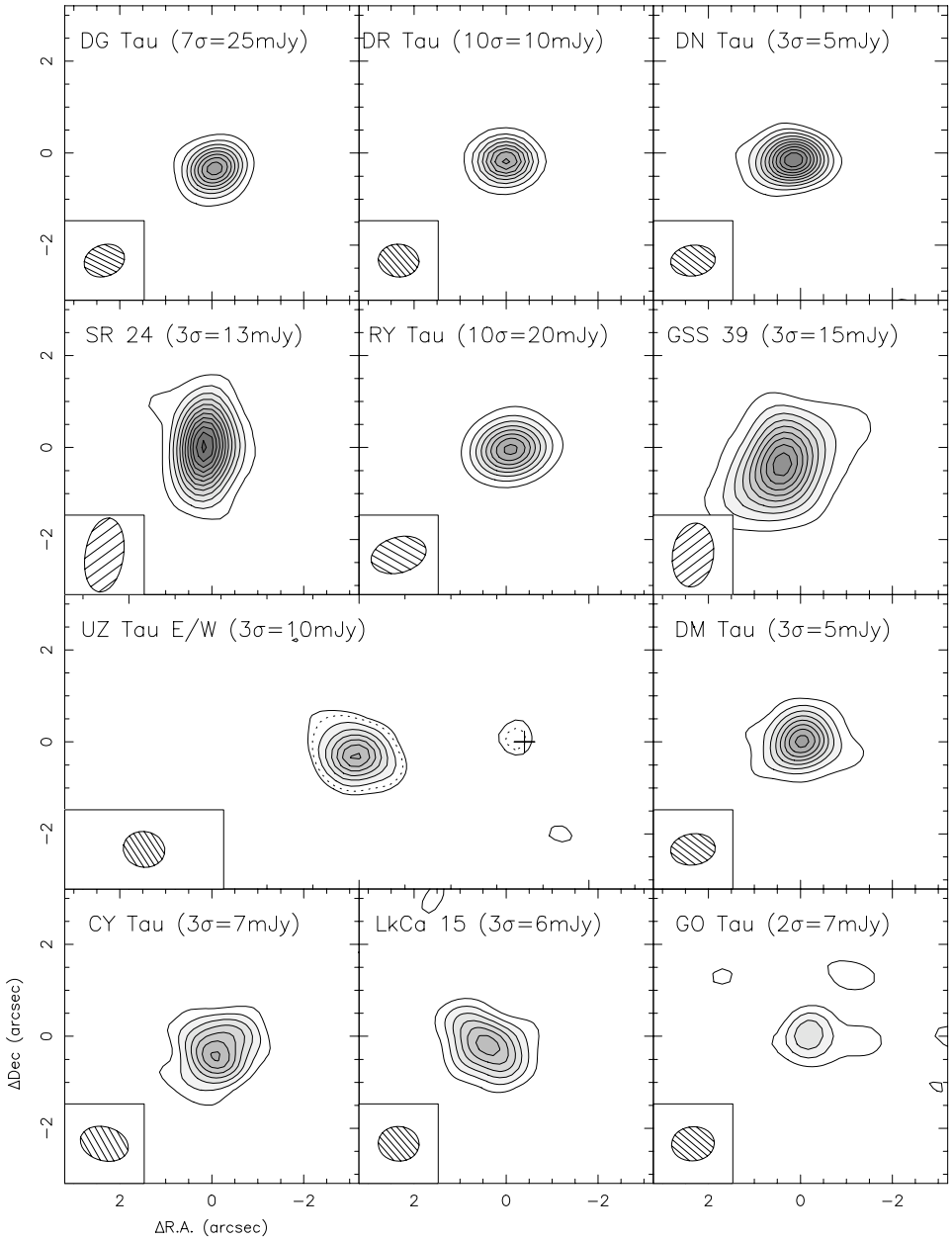

Figure 1. 1.3 mm dust continuum images of the disks observed with CARMA. Contours start at the significance levels given in each panel and are separated by that same amount. The exception is UZ Tau E/W where a cross indicates the position of UZ Tau W and the dotted contour corresponds to the 4σ level. Beam sizes and P.A. are listed in Table 2. Integrated fluxes and source sizes are given in Table 3.

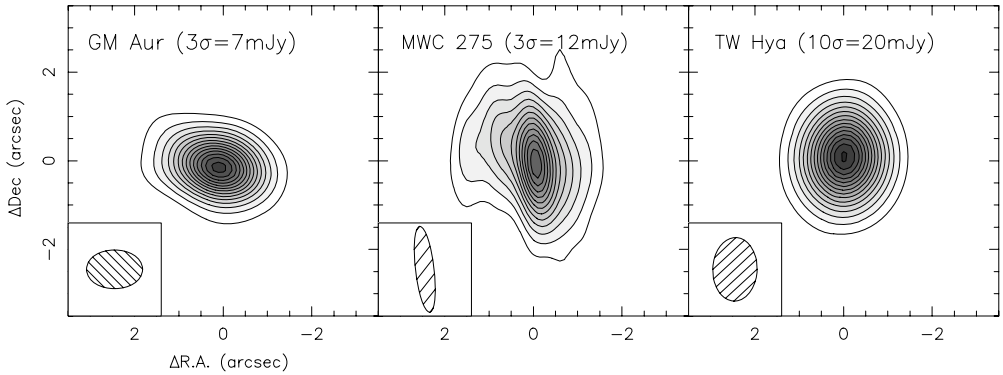

Figure 2. 1.3 mm dust continuum maps of GM Aur, TW Hya and MWC 275 (from Hughes et al. 2008; Isella et al. 2007). For GM Aur and MWC 275 contours begin at the 3σ level and are separated by the same amount. For TW Hya contours start at and are separated by the 10σ level. Beam sizes and P.A. are listed in Table 2. Integrated fluxes and source sizes are given in Table 3.

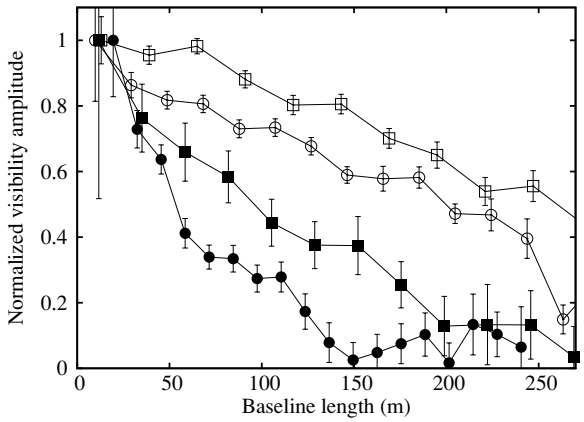

Figure 3. Normalized visibility amplitude as a function of baseline length for DR Tau (open squares), RY Tau (open circles), LkCa 15 (filled squares), and GSS 39 (filled circles).

out on a baseline of 150 m, corresponding to an angular scale of about 1.″8, while the most compact, DR Tau (empty squares), is resolved out only on a baseline of about 400 m, corresponding to an angular scale of ∼0.″7. RY Tau (empty circles) and LkCa 15 (filled squares) are intermediate cases, resolved on angular scales of 0.″8 and 1″, respectively.

Given the high S/N ratio of the observations and the good image quality, the differences in the dust emission morphology may be reasonably attributed to different radial dust properties. Assuming that the dust emission is optically thin (as discussed in Section 6.2 this is a good approximation for most of our objects), the observed surface brightness is proportional to the emitted flux expressed by

$$F_\nu(R) \propto \Sigma_d(R) \cdot k_\nu(R) \cdot T(R), \tag{1}$$

where Σ_d is the dust surface density, ν is the frequency of the observation, k_ν is the dust opacity at the frequency ν, T is the dust temperature, and R is the orbital radius. Once corrected for the stellar distance, the disk inclination and the synthesized beam shape, different surface brightness profiles can result from different radial profiles of the dust density, opacity, and/or temperature.

In the following, we will compare the observed disk emission with theoretical models to (1) derive the dust properties, particularly density and temperature, from the available observations, (2) quantify the differences between disks, and (3) investigate the origin of the different dust emission morphologies.

5. DISK MODEL AND DATA ANALYSIS

To analyze the observed disk emission we compare the measured complex visibilities with a theoretical model based on the *two layer* approximation (Chiang & Goldreich 1997) and on the similarity solution for the disk surface density of a thin Keplerian viscous disk (Lynden-Bell & Pringle 1974; Pringle 1981; Hartmann et al. 1998). The basic properties of the model are summarized in Section 5.2.

The disk model that best fits the observations is found by adopting χ^2 as the maximum likelihood estimator, where χ^2 is defined by

$$\chi^2 = \sum \left[\left(\mathrm{Re}_o^2 - \mathrm{Re}_t^2\right) + \left(\mathrm{Im}_o^2 - \mathrm{Im}_t^2\right) \right] \cdot w; \tag{2}$$

Re and Im are the real and imaginary part of the observed (suffix $_o$) and theoretical (suffix $_t$) complex visibilities. The weight w of each data point in the uv plane is given by

$$\frac{1}{\sqrt{w}} = \sigma = \frac{2k_b T_{sys}}{\eta_s \eta_a A \sqrt{2\Delta\nu\tau_{\mathrm{acc}}}} \tag{3}$$

where k_b is Boltzmann's constant, T_{sys} is the system temperature, A is the antenna area, $\Delta\nu$ is the band width, τ_{acc} is the integration time on source, and η_s and η_a are the system and antenna efficiencies, respectively. To minimize χ^2 and evaluate the constraints on the model parameters we use a Markov Chain Monte Carlo method as described in Appendix B.

5.1. Disk Surface Density

The most common approach to derive the disk surface density distribution from millimeter and submillimeter observations has been to adopt a power-law parameterization of Σ in the form

$$\Sigma(R) = \Sigma_1 \left(\frac{R_1}{R}\right)^p, \quad \text{with} \quad R_{\mathrm{in}} < R < R_{\mathrm{out}}, \tag{4}$$

where Σ_1 is the surface density value at an arbitrary radius R_1, and R_{in} and R_{out} are the disk inner and outer radii. This parameterization was initially motivated by the empirical results of Hayashi (1981), who derived a power-law surface density distribution for the solar nebula with $p = 1.5$ between 0.35 and 36 AU. This surface density parameterization has been recently revised to accommodate a number of theoretical and observational issues. First, there is no physical justification for a power-law disk surface density in terms of disk formation and evolution (see, e.g., Hueso & Guillot 2005). Moreover, such a distribution must be artificially limited between an inner and outer disk radius to obtain a finite disk mass. In addition, it has been demonstrated that the power-law parameterization fails to explain the differences in the radial extensions of the dust and the gas emission that are observed in a number of intermediate mass pre-main-sequence stars (Piétu et al. 2005; Isella et al. 2007; Hughes et al. 2008, hereafter H08). Independently it has been suggested that the gas distribution in the early solar system would be better explained by a surface density distribution of the form $\Sigma(R) \propto R^{-1/2} \times \exp(-R^{3/2})$ (Davis 2005).

Following H08, we adopt the similarity solution of the surface density of a thin Keplerian disk subject to the gravity of a point mass M_* (Pringle 1981; Lynden-Bell & Pringle 1974) in the form presented by Hartmann et al. (1998):

$$\Sigma(r, t) = \frac{C}{3\pi\nu_1 r^\gamma} \tilde{t}^{-\frac{(5/2-\gamma)}{(2-\gamma)}} \exp\left[-\frac{r^{(2-\gamma)}}{\tilde{t}}\right] \tag{5}$$

where C is a normalization constant, r is the stellocentric distance expressed in the units of a radial scale factor R_1 ($r = R/R_1$), ν_1 is the disk viscosity at radius R_1, γ is the slope of the disk viscosity $\nu(R) \propto R^\gamma$, $\tilde{t}$ is the non-dimensional time, $\tilde{t} = t/t_s + 1$, t is the age of the disk, and t_s is the disk viscous time at the radius R_1 defined by

$$t_s = \frac{1}{3(2-\gamma)^2} \frac{R_1^2}{\nu_1}. \tag{6}$$

Based on Equation (5) we demonstrate in Appendix C that R_1 is the radius containing 63% of the disk initial mass (at $t = 0$).

As pointed out by H08, this form of the surface density has the particular characteristic of falling off exponentially at large disk radii, thereby providing sufficiently dense gas in the outermost

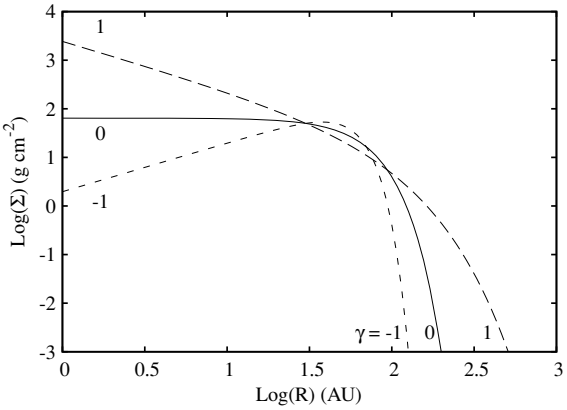

Figure 4. Disk surface density $\Sigma(R)$ as defined by Equation (9) for $\gamma = -1$, 0, and 1. The transition radius and the normalization are fixed at $R_t = 30$ and $\Sigma_t = 50$ g cm^{-2}.

disk regions to explain the observed radial extent of the gas emission. Moreover, since the similarity solution relates the surface density in Equation (5) to the age of the system, we can now investigate the details of disk evolution using our millimeter wave observations of the disk emission.

The surface density as expressed by Equation (5) includes a significant number of unknown quantities, C, ν_1, γ, t_s, and R_1, which cannot be constrained by the observations. A form more suitable for model fitting can be written by taking the derivative of Equation (5) with respect to time and introducing the mass flow

$$\dot{M}(r,t) = C\tilde{t}^{-\frac{(5/2-\gamma)}{(2-\gamma)}} \exp\left[-\frac{r^{(2-\gamma)}}{\tilde{t}}\right] \times \left[1 - \frac{2(2-\gamma)r^{(2-\gamma)}}{\tilde{t}}\right]. \quad (7)$$

Since disk evolution is governed by the conservation of the total angular momentum, the disk must expand while matter is accreting on the central star. Thus $\dot{M}$ must change sign at a *transition radius*, R_t, where

$$R_t \equiv R_1 \left[\frac{\tilde{t}}{2(2-\gamma)}\right]^{1/(2-\gamma)}. \quad (8)$$

The resulting mass flow is directed inward for $R < R_t$ (accretion) and outward (expansion) for $R > R_t$.

The surface density Σ can be rewritten in the form

$$\Sigma(R,t) = \Sigma_t \left(\frac{R_t}{R}\right)^{\gamma} \times \exp\left\{-\frac{1}{2(2-\gamma)}\left[\left(\frac{R}{R_t}\right)^{(2-\gamma)} - 1\right]\right\} \quad (9)$$

where we adopt the physical radius R and group all the other unknown quantities within Σ_t (i.e., the surface density at the radius R_t). Figure 4 displays the behavior of the surface density for different values of γ. When $\gamma = 0$, Equation (9) becomes a Gaussian law, while for negative γ the surface density has a maximum at

$$R_{\max} = R_t \times (-2\gamma)^{1/(2-\gamma)}. \quad (10)$$

Our new spatially resolved observations enable us to constrain Σ_t, R_t, and γ and define the disk surface density distribution.

5.2. Disk Structure and Emission

The flux emitted by the circumstellar dust can be computed by solving for the structure of a passive Keplerian disk (i.e., one that is heated only by the stellar radiation) adopting the *two-layer* approximation of Chiang & Goldreich (1997). If the disk is vertically optically thick to the stellar radiation, its thermal structure is characterized by a surface layer temperature T_s, which is appropriate for regions where the optical depth to the stellar radiation is < 1, and by a disk interior temperature T_i, characteristic of deeper disk regions. Both temperatures can be calculated as function of the orbital radius R by iterating on the vertical disk structure (see Dullemond et al. 2001). Assuming hydrostatic equilibrium between the gas pressure and the stellar gravity, the disk has a flared geometry with the opening angle increasing with the distance from the star and the vertical gas distribution expressed by a Gaussian law normalized to the surface density distribution described by Equation (9).

Due to the radial exponential fall-off of the disk surface density, the very outermost disk regions are optically thin to the stellar radiation and the *two-layer* approximation can not be applied. For densities typical of TTS disks, the transition to this optically thin regime occurs at a radius R_d which is much larger than the transition radius R_t. Given the dust density and temperature for $R > R_d$, we adopt R_d as the disk outer radius with negligible effects on the strength of the overall dust emission.

Once the disk thermal structure is known, the continuum dust emission can be computed by combining the flux arising from the disk interior F_ν^i with the flux from the disk surface layer F_ν^s. These are expressed respectively by

$$F_\nu^i = 2\pi \cos i \int_{R_{\rm in}}^{R_d} \left\{1 - \exp\left[\frac{-\Sigma(R)k_\nu^i}{\cos i}\right]\right\} \times B_\nu[T_i(R)] \frac{R}{d^2} dR \quad (11)$$

and

$$F_\nu^s = 2\pi \int_{R_{\rm in}}^{R_d} \left\{1 + \exp\left[\frac{-\Sigma(R)k_\nu^i}{\cos i}\right]\right\} \times B_\nu[T_s(R)]\, \Delta\Sigma(R)\, k_\nu^s \frac{R}{d^2} dR \quad (12)$$

(Dullemond et al. 2001; Chiang et al. 2001), where ν is the frequency, d is the distance to the source, i is the disk inclination with respect to the plane of the sky ($i = 0$ for face-on), $B_\nu(T)$ is the Planck function, $\Delta\Sigma$ is the column density in the disk surface, and $k_\nu^{i,s}$ are the dust opacities at the disk mid plane and surface, as discussed in the next section. The disk inner radius $R_{\rm in}$ is fixed at the dust evaporation distance and varies between $\sim$0.03 and $\sim$0.5 AU for the stellar luminosities characteristic of our sample (Isella & Natta 2005; Isella et al. 2006).

5.3. Dust Opacity

To calculate the disk structure and emission we adopt the optical constants of astronomical silicates and carbonaceous materials (Weingartner & Draine 2001; Zubko et al. 1996). The dust opacity is calculated assuming compact spherical grains and adopting the fractional abundances used by Pollack et al. (1994) and results in a dust/gas ratio close to 0.01. We assume a grain size distribution of the form $n(a) \propto a^{-q}$ between 0.01 μm and 10 cm, where q is a free parameter of the model. Figure 5 shows the dust opacity at 1.3 mm ($k_{1.3}$, dashed line) and the slope β of the dust opacity ($k_\lambda \propto \lambda^{-\beta}$) calculated between 1 and 7 mm (solid line), as a function of the slope of the grain size distribution q. $k_{1.3}$ reaches a maximum value of 1.9 cm^2 *per gram of dust* for $q = 3.9$ and decreases to values smaller than

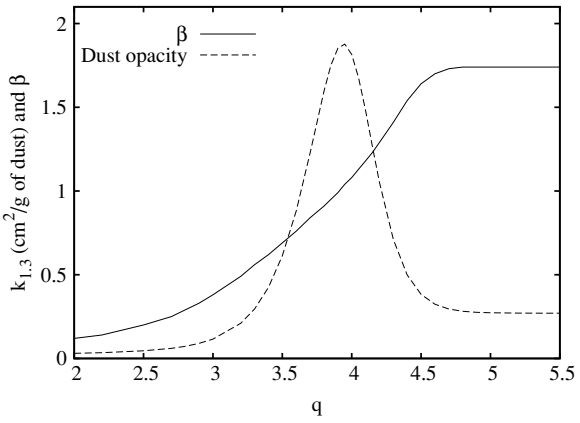

Figure 5. Dust opacity at 1.3 mm ($k_{1.3}$) and the slope β of the dust opacity at millimeter wavelengths as a function of the slope, q, of the grain size distribution $n(a) \propto a^{-q}$. A minimum grain radius of 0.01 μm and a maximum grain radius of 10 cm are assumed.

0.4 cm^2 *per gram of dust* for $q < 3.4$ and $q > 4.5$. The slope β increases with q, and varies between $\beta = 0.1$ for $q = 2$ (when the opacity is dominated by 10 cm size grains) to $\beta = 1.7$ for $q > 4.5$ (when the opacity is dominated by submicron grains; see Natta et al. 2007 and references therein for more details on the variation of β with the grain size and composition).

To solve for the disk structure, we adopt different values of q for the disk interior and the disk surface layer. To a first approximation, as long as the disk is optically thick to the stellar radiation neither the disk structure nor the millimeter-wave dust emission depends on the assumed dust opacity in the disk surface layer. We therefore fix the value of q at 5 in the disk surface so that the opacity is dominated by the submicron grains which are generally required to explain the silicate features observed between 10 and 20 μm (Furlan et al. 2006). The value of q in the disk interior is a free parameter and is chosen so as to reproduce the measured slope α of the spectral energy distribution (SED; $F_\nu \propto \nu^\alpha$) between 0.8 and 7 mm. The resulting values of α, q, $k_{1.3}$, and β are presented and discussed in Section 6.1.

It is important to emphasize that since we are analyzing the spatially resolved dust emission observed at a single wavelength, we cannot disentangle the radial variation of the dust opacity from the variation of dust surface density. In effect, the observations constrain the product $k_{1.3}(R) \times \Sigma(R)$ (see Section 4). Since the radial variation of the dust opacity has not been quantified observationally, we assume that $k_{1.3}$ is constant throughout the disk.

Table 4
Dust Properties

Object	α	β	$a_{max} = 100$ mm		$q = 3$	
			q	$k_{1.3}$[a]	a_{max}[b]	$k_{1.3}$[a]
CY Tau	2.6	0.7	3.5	0.6	1	3.9
DG Tau	2.3	0.5	3.1	0.2	22	0.39
DM Tau	2.9	1.1	4.0	1.8	0.16	6.6
DN Tau	2.7	0.8	3.7	1.2	0.55	5.6
DR Tau	2.4	0.6	3.3	0.3	1.9	2.6
GO Tau	3.4	1.5	4.5	0.4	0.13	6.8
LkCa15	3.5	1.7	4.7	0.3	0.13	6.8
RY Tau	2.5	0.7	3.5	0.6	1.0	3.9
UZ Tau E	2.6	0.7	3.5	0.6	1.0	3.9
GM Aur	3.1	1.3	4.2	1.1	0.14	6.7
GSS 39	2.8	0.9	3.8	1.6	0.3	7.4
SR 24	2.6	1.1	4.0	1.8	0.16	6.6
TW Hya	2.5	0.8	3.6	0.9	0.55	5.6
MWC 275	2.9	1.0	3.9	1.9	0.185	7.0

Notes.
[a] 1.3 mm dust opacity is in cm^2 per gram of dust.
[b] Dust size is in mm.

6. RESULTS OF THE MODEL FITTING

The model comparison with observations is described in Appendix B. For all the objects we obtain good fits to the observations, with reduced χ^2 close to 1. The dust properties adopted in the model fitting are presented in the Table 4, which list the slope q of the grain size distribution (Column 4) and the corresponding dust opacity at 1.3 mm $k_{1.3}$ (Column 5). Disk inclination, the position angle of the projected disk major axis, the transition radius R_t, the surface density Σ_t at R_t, and the value of γ corresponding to the best-fit models are shown in Table 5. The last two columns of Table 5 show the total disk mass and the radius R_d at which the disk becomes optically thin to the stellar radiation. For each object, the disk emission between 0.5 and 7 mm is shown in Figure 6. The radial profiles of the disk surface density $\Sigma(R)$, the cumulative disk mass $M_d(R)$, the disk surface and interior temperature profiles $T_{s,i}(R)$, and the cumulative emission at 1.3 mm $F_{1.3}(R)$ are shown in Figure 7. The comparison between the observed and the best-fit model

Table 5
Model Fitting Results

Object	i (deg)	P.A. (deg)	R_t (AU)	Σ_t (g cm^{-2})	γ	Log(M_d) ($M_\odot$)	R_d (AU)
CY Tau	51 ± 7	148 ± 8	55 ± 5	10 ± 2	−0.3 ± 0.3	−1.16	197
DG Tau	18 ± 10	15 ± 27	21 ± 1	608 ± 24	−0.5 ± 0.2	−0.38	89
DM Tau	25 ± 10	3 ± 70	86 ± 32	1.5 ± 0.8	0.8 ± 0.1	−1.63	481
DN Tau	30 ± 10	61 ± 18	28 ± 3	13 ± 3	0.0 ± 0.5	−1.73	125
DR Tau	37 ± 3	98 ± 5	21 ± 1	80 ± 4	−0.3 ± 0.5	−1.20	86
GO Tau	25 ± 25	90 ± 90	110 ± 80	4 ± 2	0.7 ± 0.4	−1.15	670
LkCa15	58 ± 4	48 ± 4	60 ± 4	31 ± 7	−0.8 ± 0.4	−0.72	241
RYTau	60 ± 3	25 ± 3	25 ± 1	58 ± 4	−0.1 ± 0.4	−1.19	112
UZTauE	43^{+10}_{-20}	70 ± 5	43 ± 10	12 ± 5	0.8 ± 0.4	−1.32	260
GM Aur	51 ± 2	55 ± 2	56 ± 1	12 ± 1	0.4 ± 0.1	−1.14	350
GSS39	46 ± 7	111 ± 7	66 ± 10	4.7 ± 1.6	0.5 ± 0.2	−1.36	390
SR24	65 ± 7	48 ± 4	20 ± 4	50 ± 10	0.1 ± 0.3	−1.43	120
TW Hya	11 ± 2	65 ± 3	17.5 ± 0.5	60 ± 2	$-0.3^{+0.1}_{-0.4}$	−1.49	73
MWC 275	51 ± 2	21 ± 4	85 ± 3	2.7 ± 1.2	0.3 ± 0.1	−1.41	520

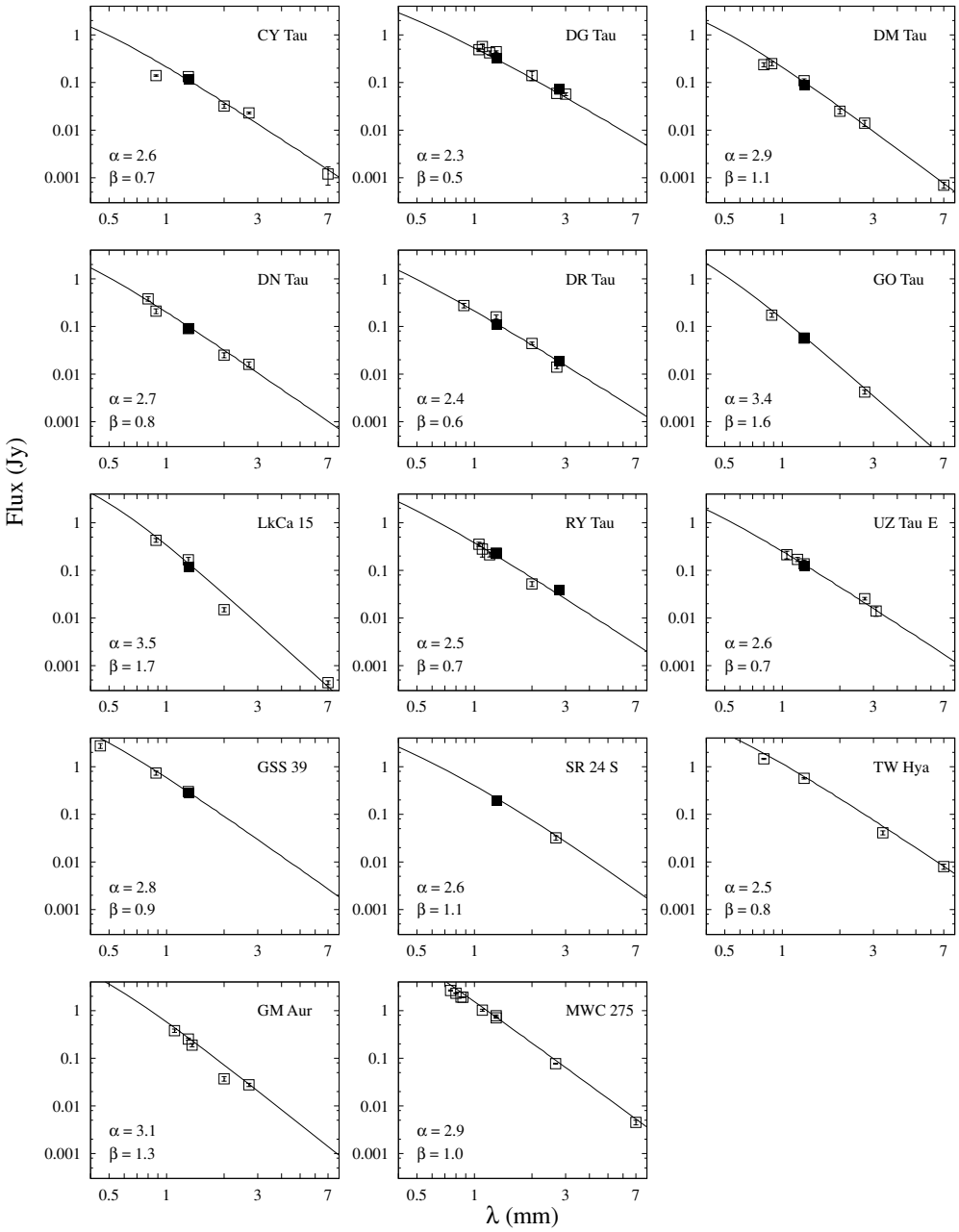

Figure 6. Flux density distribution of the observed sample between 0.4 and 8 mm. Filled squares correspond to the CARMA observations discussed in this paper, and open squares correspond to measurements available in the literature (Dutrey et al. 1996; Kitamura et al. 2002; Andrews et al. 2005; Rodmann et al. 2006; Isella et al. 2007). The solid curves correspond to disk models that best fit the spatially resolved observations at 1.3 mm (see Table 5). For each object the values of α and of the dust opacity slope β are indicated in the relative panel.

visibility profiles are shown in Figure 8, and the residuals, defined as the difference between the observed maps of the 1.3 mm dust emission and the models, are shown in Figure 9.

6.1. Properties of the Dust

Figure 6 shows the spatially integrated fluxes of the observed disks between 0.5 and 7 mm. CARMA observations are represented by filled squares while open squares depict data from the literature. The solid curves show the best-fit models characterized by the values of spectral index α ($F_\nu \propto \nu^\alpha$), slope β of the dust opacity, slope q of the grain size distribution, and dust opacity at 1.3 mm $k_{1.3}$ reported in Column 2–5 of Table 4. We derive values of α between 2.4 (DG Tau) to 3.5 (LkCa 15), which lead to values of β between 0.5 and 1.7. If the disk emission is optically thin at 1.3 mm, α and β are tightly correlated with $\beta = \alpha - 2$ (e.g., Beckwith & Sargent 1991). In practice, the denser regions of the disk are partially optically thick at 1.3 mm and $\beta \geqslant \alpha - 2$. The difference between β and $\alpha - 2$ depends on the ratio of optically thick to optically thin emission from the disk and is only few percent in CY Tau, DN Tau, UZ Tau E, and GSS39. However, it increases to about 20% in SR 24 S and DG Tau, where the disks are optically thick to the 1.3 mm emission within a radius of 17 AU and 25 AU, respectively.

The dust opacity $k_{1.3}$ obtained by the SED fitting strongly depends on the assumed grain size distribution discussed in Section 5.3. Actually, we can reproduce the observed spectral

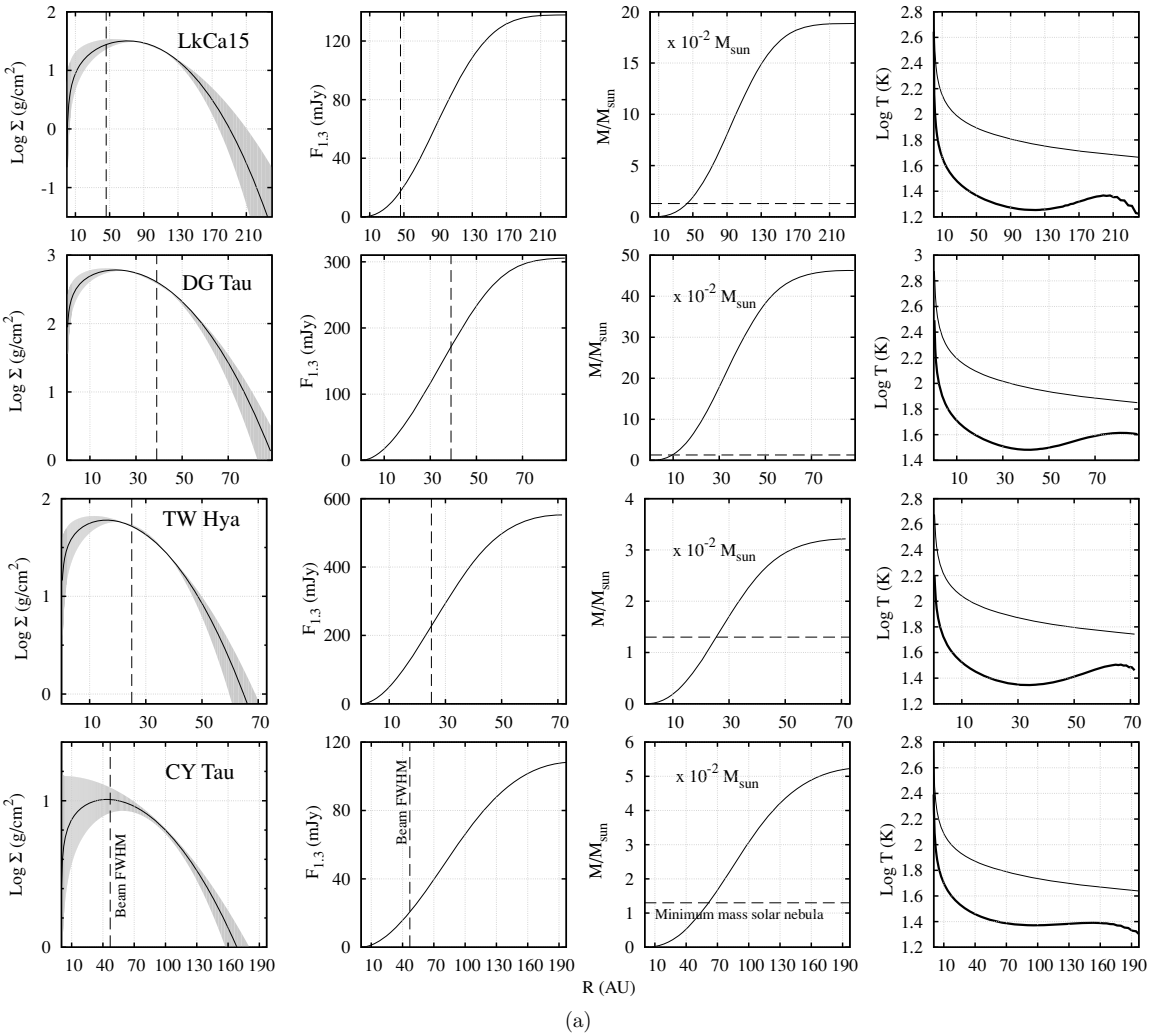

(a)

Figure 7. Radial profiles of the disk surface density, cumulative flux at 1.3 mm, cumulative mass and disk temperature for the best-fit model from Table 5. The shaded region in the surface density panels corresponds to the 1σ uncertainties obtained from MCMC fitting. The vertical dashed lines indicate the spatial resolution of the observations. In the panels of Column 3, the horizontal dashed line at 0.02 $M_{\odot}$ is the minimum mass solar nebula (Hayashi 1981), and the disk cumulative mass is expressed in units of $10^{-2} M_{\odot}$. The disk interior temperature T_i is represented by a thick line in the panels of Column 4 while the disk surface layer temperature is a thin line.

indexes α with very different dust opacities if we fix the slope of the grain size distribution q and keep $a_{\rm max}$ as a free parameter. Values of $a_{\rm max}$ and $k_{1.3}$ for the case $q = 3$ are shown in the last two columns of Table 4. This latter grain size distribution leads to dust opacities larger than the case with fixed $a_{\rm max}$ and variable q by a factor 2–20. As a consequence, much smaller surface densities and disk masses are required to reproduce the observed dust emission.

Independently of the assumed grain size distribution, values of $\beta \lesssim 1$ imply that the dust opacity is strongly influenced by dust grains larger than 1 mm (e.g., Natta et al. 2007). This suggests that the circumstellar dust around CY Tau, DG Tau, DN Tau, DR Tau, RY Tau, UZ Tau E, GSS 39, and TW Hya has undergone important grain growth processes. However, the small value of the spectral index for DG Tau can now be probably explained by the strong contribution of the optically thick emission at 1.3 mm. By contrast, the dust properties in LkCa 15 and GO Tau are more similar to that found in the interstellar medium. Moreover, disks with small value of β tend to be characterized by small value of γ and therefore to steeper surface density profiles for $R > R_t$. This suggests that the dust surface density may be correlated with the dust properties and in particular that small and large dust grains might have different radial density distributions, as suggested by recent theoretical models of growth and radial migration of dust grains in protoplanetary disks (Brauer et al. 2008).

6.2. Radial Profile of the Surface Density

In the panels of the first and second columns of Figure 7 we show for each object the surface density and the cumulative flux at 1.3 mm (solid line), the 1σ uncertainty range (shaded region) and the spatial resolution provided by our interferometric observations (vertical dashed line). The dust emission coming from spatially resolved disk regions varies from about 85% (CY Tau, LkCa 15, MWC 275, GSS 39) to less than 30% (DR Tau, SR 24 S) of the total flux. As a consequence, the constraints on R_t, γ, and Σ_t vary from few percents to about 30%–40%.

The derived transition radii range from 17.5 and 110 AU. For the assumed dust opacities and stellar distances, the radius R_d at which the disk becomes optically thin to the stellar radiation—in effect the disk outer radius (Section 5.2)—varies from 73 AU in the case of TW Hya to 670 AU for GO Tau. These values are close to the disk outer radii inferred from the analysis of the optically thick CO emission (Simon et al. 2000), but larger

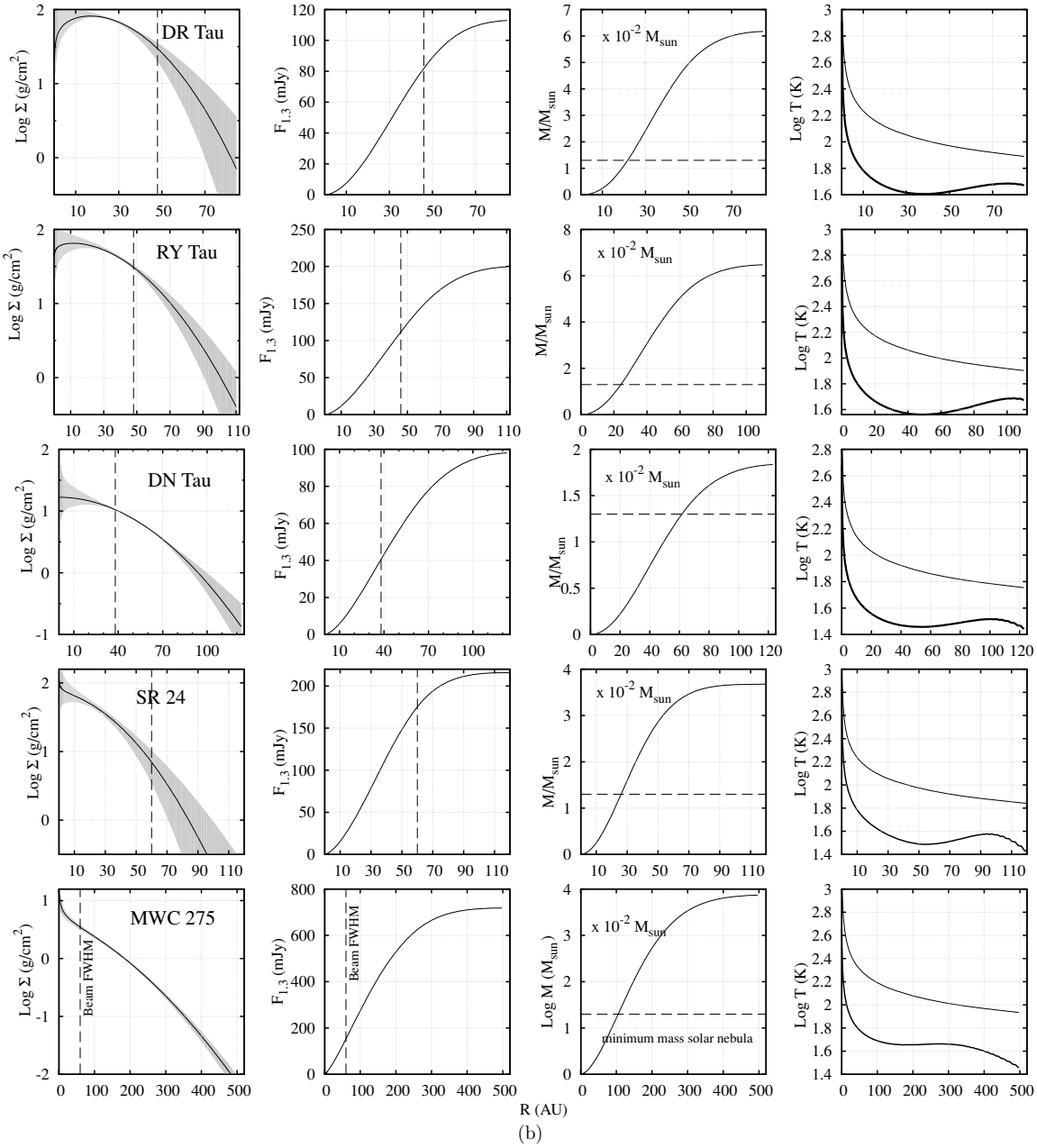

(b)

Figure 7. (Continued)

than existing determinations of the disk outer radii based on power-law surface density models (Andrews et al. 2007). In the case of MWC 275, we find $R_d = 520$ AU. This radius is in very good agreement with the gas extent inferred from the CO line emission but it is twice as large as the disk outer radius implied by the same observations if a power-law surface density disk model is adopted (Isella et al. 2007). It appears that there is in fact *no* discrepancy between the radial extents of the gas and dust emission. The outer radii determination of the dust extent based on the exponential fall-off for the surface density are quite comparable with the radii derived from observations of the CO emission (see also H08).

From Equation (9), it is clear that the disk surface density is characterized by γ, which ranges from -0.8 to 0.8. For $R \gtrsim R_t$, radial density profiles become steeper with decreasing γ, as shown in Figure 4. This is further illustrated by the plots of Σ in the panels of the first column of Figure 7. In Figure 7(a), LkCa 15, CY Tau, DG Tau, and TW Hya have negative values of γ with a probability of at least 68% (1σ, see Appendix B). From Equation (10) (Section 5.1), the corresponding surface densities have maxima at 89, 41, 21, and 13 AU, respectively. For LkCa 15, the CARMA observations clearly resolve the surface density maximum and the almost flat profile of Σ between 50 and 100 AU. For the other objects the predicted maxima lie inside the resolution of our observations. Disks with values of $\gamma \sim 0$ are shown in Figure 7(b), and for $\gamma > 0$ in 7(c). For almost all disks, Σ is well constrained for $R \gtrsim 40$ AU. For DR Tau and SR 24 S, almost 80% of the observed emission arises from the innermost spatially unresolved disk region so that the disk structure is poorly constrained. The structure of GO Tau disk is also poorly constrained due to the low S/N ratio of the observations.

The inferred disk structure depends weakly on the adopted grain size distribution if the SED is used to constrain the dust opacity. In fact, the disk mid plane temperature $T_i(R)$ varies by

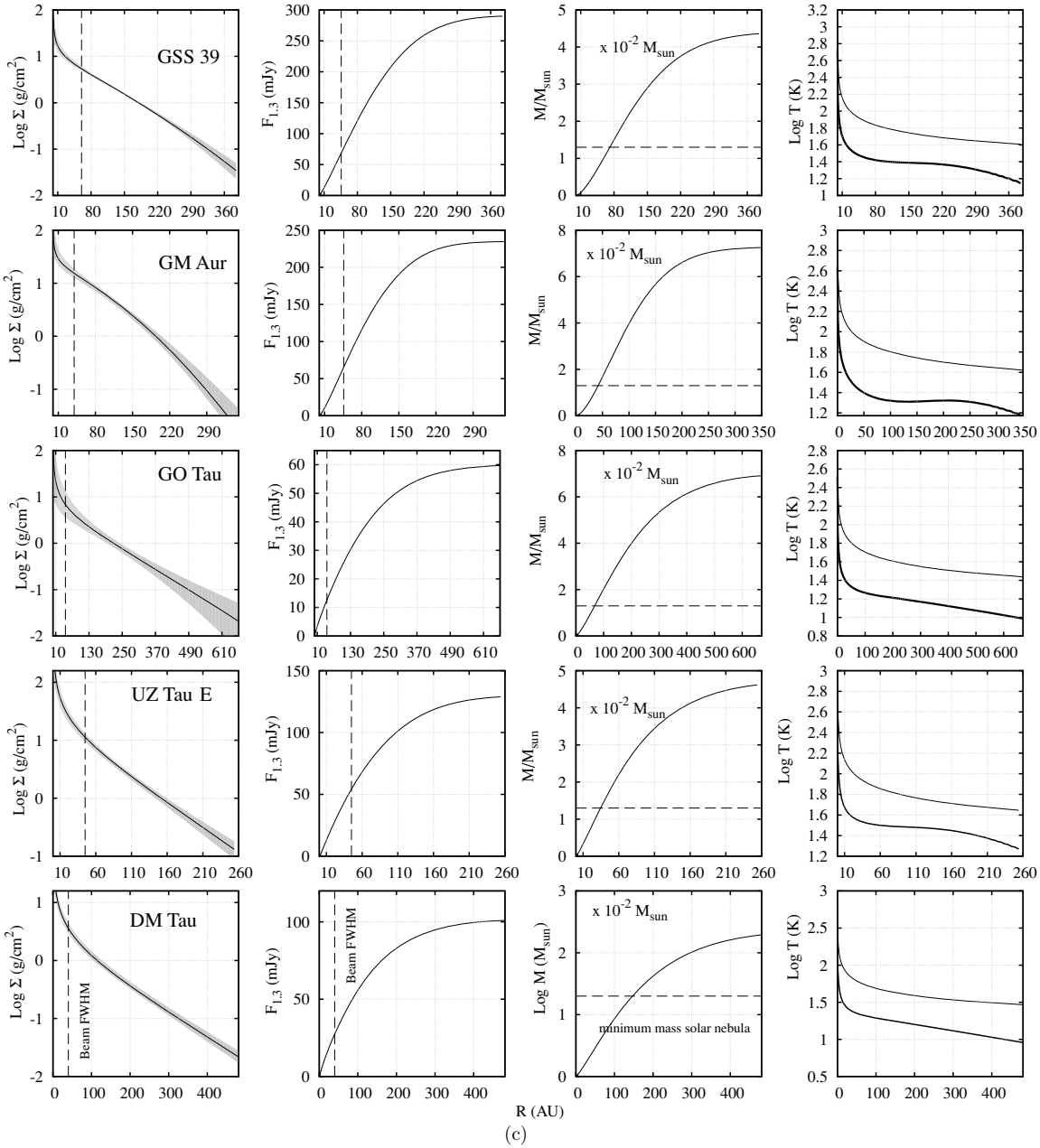

(c)

Figure 7. (Continued)

less than 5% between the two different grain size distribution models shown in Table 4. Consequently, since $\Sigma(R) \propto T^{-1}(R)$, 5% is also the maximum variation observed in the profile of the surface density. We obtained model fits for a subset of the disks using the alternative grain size distribution listed in Table 4, and have verified that the variations on γ and R_t are much smaller that the respective uncertainties.

6.3. Disk Mass

The radial integration of the disk surface density leads to the cumulative disk mass $M(R)$ presented in the panels in Column 3 of Figure 7, and to the total disk mass M_d in Table 5. For the adopted grain size distribution and dust/gas ratio (Section 5.3), M_d varies by more than an order of magnitude from $\sim$0.02 to $\sim$0.4 $M_\odot$, with uncertainties between 20% and 200% depending on how well Σ is constrained. In the case of DG Tau, the mass of the disk is comparable with the stellar mass. Note, however, that stellar masses derived using DM97 stellar evolution models are probably a lower estimate of the real stellar mass. Indeed, the disk mass is only 35% of the stellar mass if Baraffe et al. (1998) models are used to derive the stellar mass from the H–R diagram (see Appendix A). Disk mass is 15% of the mass of the parent star for DN Tau and GM Aur, while it is only a few percent for all the other objects.

Disk masses strongly depend on the dust opacity at 1.3 mm which may vary by a large factor if a different grain size distribution is adopted. The case $q = 3.0$ discussed is Section 6.1 leads to disk masses between a factor 2 and 20 smaller than what discussed above. This introduces an additional large uncertainty on the disk masses derived from millimeter-wave observations.

As shown in the cumulative mass plots, most of the disk mass is concentrated in the outermost disk regions, independent of the exact surface density profile. By contrast, since the disk scale

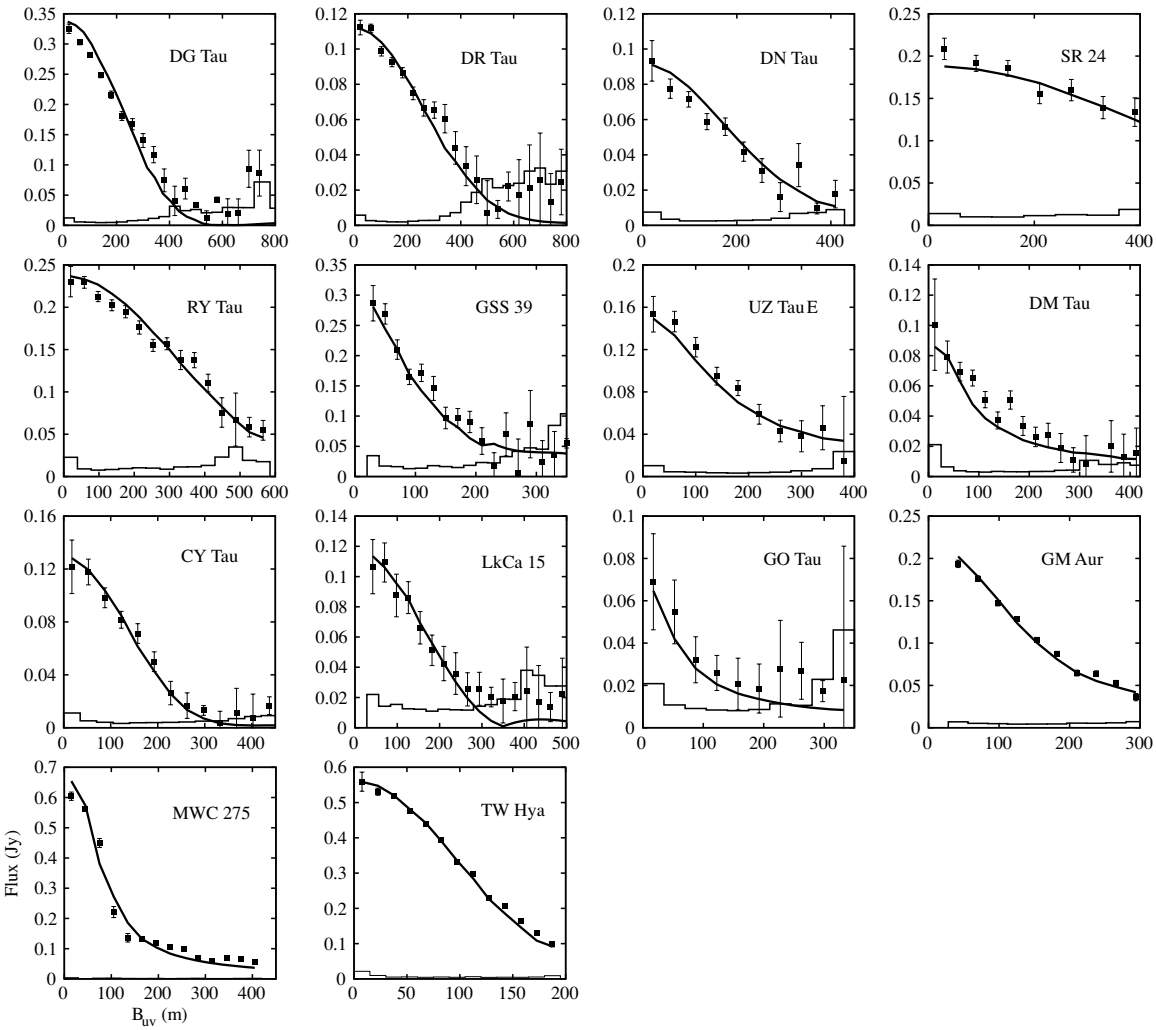

Figure 8. Comparison between the observed correlated flux (dots) and the best-fit model prediction (solid line) as a function of the baseline length deprojected using disk inclinations and position angles listed in Table 5. The histogram in the lower part of each panel shows the expected signal in case of zero flux.

height $H(R)$ increases with distance from the star, the dust+gas volume density in the disk mid-plane [$\rho_0 \propto \Sigma(R)/H(R)$] is at a maximum close to the inner disk radius. A comparison of M_d with the minimum mass of the solar nebula (0.02 $M_\odot$; see Figure 7) shows that this amount of material is contained within radii ranging from ∼10 AU (for DG Tau) to ∼60 AU (for DM Tau, MWC 275). These values are not too far from the minimum mass solar nebula outer radius of 36 AU postulated by Hayashi (1981). We will return to this point in Section 7.3.

6.4. Disk Temperature

The panels in the last column of Figure 7 display the radial profile of the dust temperature in the disk interior, T_i (thick line), and in disk surface layer, T_s (thin line). As discussed in Section 5.2, T_s scales roughly as $R^{-1/2}$ due to the dilution of the stellar radiation and to the variation of the Planck mean dust opacity. It varies between ∼1500 K at the disk inner radius, and 10 to 40 K at R_d, where the disk becomes optically thin to the stellar radiation in the vertical direction. Since the dust column density in the disk atmosphere is a tiny fraction ($\sim 10^{-4}$) of the total disk surface density, the contribution to the observed millimeter emission from the disk atmosphere is negligible (see Equation (12)).

Inside a radius of 50–100 AU, the dust temperature T_i in the deeper disk region also scales as $R^{-1/2}$, as expected for an irradiated optically thick disk (Kenyon & Hartmann 1995). At larger distances the dust density is low enough that the disk interior becomes progressively optically thin to the emission of the disk atmosphere (which heats up the disk interior) and to its own thermal emission (which cools the disk interior). The resulting effect is that the temperature profile deviates from the $R^{-1/2}$ relation. The deviation is larger in disks characterized by small values of γ and a correspondingly steeper decrease in the surface density (see Figures 7(a) and (b)). In these objects, the temperature of the disk region that dominates the observed millimeter emission assumes almost constant values between 20 and 40 K. By contrast, T_i decreases monotonically in disks with the highest γ (i.e., DM Tau, GO Tau, and UZ Tau E). In no cases does the disk temperature fall below 10 K which is generally assumed to be the equilibrium temperature with the interstellar radiation field.

6.5. Disk Orientation

Disk inclinations and the position angles derived from the observations are uncorrelated and randomly distributed as expected in the absence of a preferential disk orientation in space.

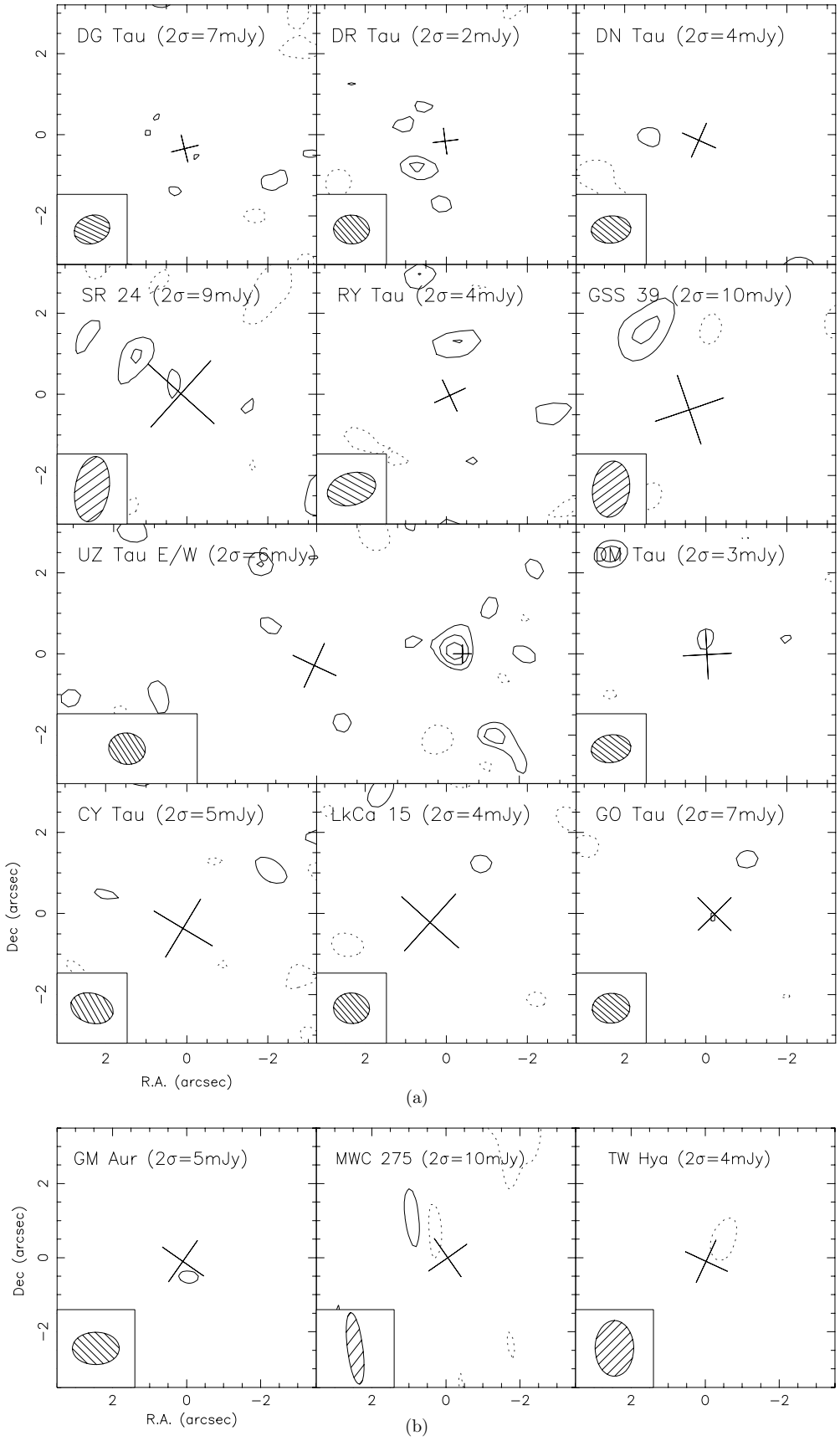

Figure 9. Maps of the residuals calculated by subtracting the best-fit model from the observations. The contours start at the 2σ level and are separated by 1σ. Cross indicates the position of the source and the orientation of the disk. The smaller cross in the UZ Tau E panel indicates the position of UZ Tau W.

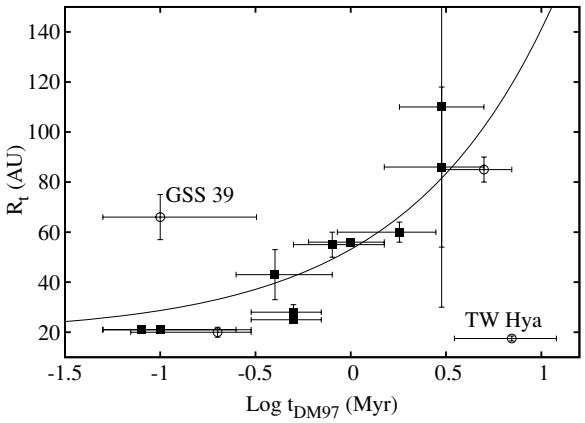

Figure 10. Disk transition radius R_t as a function of the stellar age computed using DM97 models. Filled squares show the 10 disks located in Taurus-Auriga star-forming region. For this sub sample, the correlation coefficient between R_t and the stellar age is 0.98 and the probability that the data are randomly distributed is less than 0.1%. The solid line corresponds to $R_t = R_0 + C \cdot t^{\eta}$ with $\eta = 0.5 \pm 0.4$, $R_0 = 17 \pm 10$ AU, and $C = 37 \pm 20$.

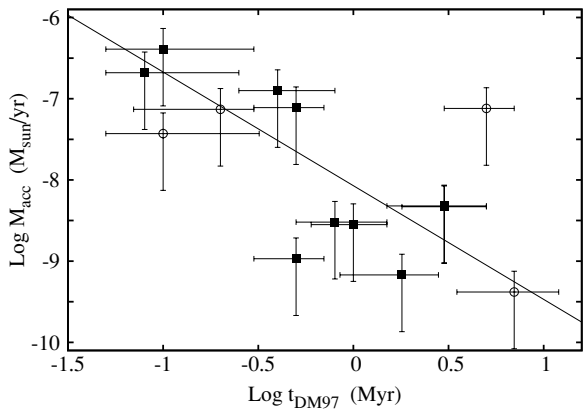

Figure 11. Mass accretion rate as a function of stellar age computed from DM97 models. Filled squares show the 10 disks located in Taurus-Auriga star-forming region. The correlation coefficient between $\dot{M}_{\rm acc}$ and the stellar age is -0.62 and the probability that the data are randomly distributed is about 2%. The solid line corresponds to $\dot{M}_{\rm acc} \propto t^{-1.4}$.

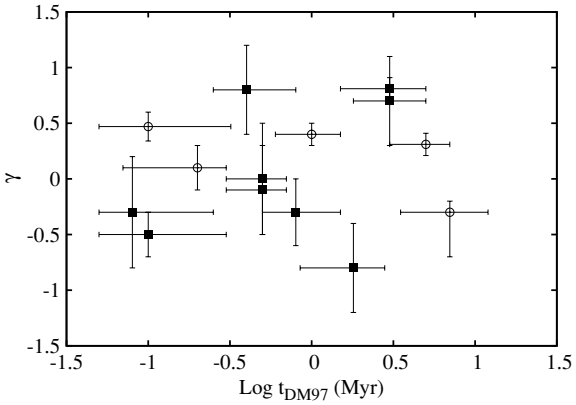

Figure 12. Variation of the parameter γ, which defines the surface density profile, with the stellar age calculated from DM97 models. The 10 disks in Taurus-Auriga are shown by filled squares.

For CY Tau, DG Tau, DN Tau, DM Tau, LkCa15, UZ Tau E, GM Aur, GSS39, SR24, TW Hya, and MWC 275 both inclinations and position angles are in agreement with published values within 2σ (Jensen et al. 1996; Dutrey et al. 1997; Simon et al. 2000; Qi et al. 2004; Piétu et al. 2006; Andrews et al. 2007; Isella et al. 2007). For GO Tau, DR Tau, and RY Tau we derive disk inclinations of $25^\circ \pm 25^\circ$, $37^\circ \pm 3^\circ$, and $60^\circ \pm 3^\circ$, respectively, considerably lower than the 66°, 72°, and 86° suggested by Andrews et al. (2007). On the other hand, our RY Tau results agree well with recent optical observations (St-Onge & Bastien 2008) suggesting that the discrepancies may be due to the lower S/N ratio of Andrews et al. (2007) observations compared with the new CARMA results.

7. DISCUSSION

From the results of Section 6, we conclude that the diversity in the surface brightness profiles observed in our 1.3 mm dust continuum maps (Section 4) is due mainly to different surface densities, $\Sigma(R)$, with the disk temperature $T_i(R)$ having only a minor effect. Of course, this assumes that the dust opacity is constant with radius, as discussed in Section 5.3. Most of the discussion below is therefore devoted to examining the dust density profiles and investigating the possible sources of the observed variations.

7.1. Disk Evolution

Figure 10 compares the disk transition radius R_t and the stellar age (from Appendix A). Over the ∼5 Myr span of our sample ages, R_t appears to increase with stellar age from about 20 to 100 AU. Applying the non-parametric Spearman rank-order test (see, e.g., Press et al. 2007), the correlation coefficient is $r = 0.42$ and the probability that the data are randomly distributed is 12%. However, limiting the analysis to the objects in Taurus-Auriga (filled squares) the correlation coefficient increases to 0.98 and the probability of a random distribution falls below 0.1%. If R_t has a power-law dependence of the form $R_t = R_0 + C \cdot t^{\eta}$, where t is the stellar age in Myr, we find that R_t increases as $\sqrt{t}$, with $\eta = 0.5 \pm 0.4$, $R_0 = 17 \pm 10$ AU, and $C = 37 \pm 20$. As shown in Figure 11, this disk expansion is accompanied by a decrease in the mass accretion rate roughly described by $\dot{M}_{\rm acc} \propto t^{-1.4 \pm 0.3}$. In this case, the Spearman test indicates that the probability that the data are randomly distributed is 2% ($r = -0.62$) both for the full sample and for the objects in Taurus-Auriga. As illustrated in Figure 12, there appears to be no correlation between γ and stellar age ($r = 0.18$).

The observed increase of the disk transition radius, R_t, and decrease of the mass accretion rate, $\dot{M}_{\rm acc}$, suggests that the our sample disks represent an evolutionary sequence. Stars with different mass, spectral type, and luminosity are accompanied by disks whose characteristics seem to vary similarly with time, i.e., they evolve in a similar way. Can we interpret this in terms of the viscous disk model of Section 5.1?

To answer this question we can start from Equation (8) and express the temporal variations of R_t as

$$R_t = R_1 \left[\frac{1}{2(2-\gamma)} \left(\frac{t}{t_s} + 1 \right) \right]^{1/(2-\gamma)} \qquad (13)$$

and from Appendix D, the mass accretion rate

$$\dot{M}_{\rm acc} = \frac{M_d(0)}{2(2-\gamma)t_s} \left(\frac{t}{t_s} + 1 \right)^{-(5/2-\gamma)/(2-\gamma)}, \qquad (14)$$

where γ is assumed to be constant with time. The values of γ derived for our sample (Table 5) lead to $R_t \propto t^{0.3-0.8}$ and

$\dot{M}_{\rm acc} \propto t^{-(1.2-1.4)}$. The agreement with the relation derived above from our observations suggests that the values of R_t and $\dot{M}_{\rm acc}$ result from viscous evolution of disks formed with similar masses and radii over a time interval of about 5 Myr.

7.1.1. Initial Disk Properties and Timescale for the Disk Evolution

The initial disk radius, R_1, the initial disk mass $M_d(0)$ and the viscous timescale at R_1, t_s, can be estimated from Equations (13) and (14). Assuming values of γ between -0.8 to 0.8, we obtain $R_1 = 25$–40 AU, $M_d(0) = 0.05$–$0.4\ M_\odot$, and $t_s = 0.1$–0.3 Myr. In Appendix C we showed that R_1 is the radius containing 63% of the initial disk mass $M_d(0)$, while about 90% of the initial disk mass $M_d(0)$ is contained within about $2R_1 = 50$–80 AU. As noted in Appendix A, stellar ages increase by a factor 3–10 if B98 models are used instead of DM97. Nevertheless, the transitional radii, R_t, and the mass accretion rates, $\dot{M}_{\rm acc}$, still correlate with the stellar ages with similar correlation coefficients. R_1 and $M_d(0)$ are influenced very little by different evolutionary models but the resulting viscous timescales are about a factor 4 larger. In the following discussion we focus on deriving constraints on the processes that govern the disk viscosity and the disk formation from R_1, $M_d(0)$, and t_s.

7.1.2. Implications for Disk Viscosity

From the disk radius R_1, the corresponding viscous timescale t_s and the parameter γ, we can derive the absolute value of the disk viscosity and its radial profile $\nu(R)$. From Section 5.1, $\nu(R)$ is expressed by

$$\nu(R) = \frac{1}{3(2-\gamma)^2}\frac{R_1^2}{t_s}\left(\frac{R}{R_1}\right)^{\gamma}. \quad (15)$$

Since different values of γ are derived from our observations of the millimeter dust emission, the disk viscosity is probably characterized by a variety of radial profiles. Thus for $\gamma > 0$ (DM Tau, GO Tau, UZ Tau E, GM Aur, GSS 39, and MWC275) the viscosity increases with radius. For $\gamma \sim 0$ (CY Tau, DN Tau, DR Tau, RY Tau, SR 24) the viscosity is virtually constant with radius, and for the few objects with $\gamma < 0$, it decreases.

The viscosity in a disk is generally attributed to some degree of turbulence that may originate from different physical processes. Two possible sources of turbulence are the magneto-rotational instability (MRI; Balbus & Hawley 1991) and gravitational instability (GI; e.g., Lodato & Rice 2004). MRI requires weak magnetized disks and a minimum ionization fraction of about 10^{-13} at 1 AU (Balbus & Hawley 2000). For the disk to be MRI active the maximum surface density must lie between 10 and 100 g cm^{-2}, depending on the ionization source (Terquem et al. 2008). This condition is satisfied in most of our objects (see Figure 7). For DG Tau, SR 24 S, and RY Tau, however, the high density at the disk mid-plane inside a radius of about 30 AU probably prevents ionization. In such regions, where the MRI cannot operate, viscosity may originate from GIs. Classically GI can be parameterized by the Q-value (Toomre 1964)

$$Q = \frac{c_s \Omega}{\pi G \Sigma(R)} \quad (16)$$

where Ω is the Keplerian angular velocity ($\Omega = \sqrt{GM_*/R^3}$) and c_s the sound of speed. When $Q \lesssim 1.5$, the disk is gravitationally unstable and develops spiral waves to transport angular momentum outward and mass inward (Lodato & Rice 2004). Adopting Equation (E2) for the sound speed in the disk, we can rewrite Q in the form

$$Q \sim 230\left(\frac{M_*}{0.5\ M_\odot}\right)^{1/2}\left(\frac{R}{10\ \rm AU}\right)^{-3/2}\Sigma(R)^{-1}T_i(R)^{1/2} \quad (17)$$

where as usual Σ and T_i are the disk surface density and interior temperature as in Figure 7. Among the observed objects, DG Tau has a gravitationally unstable disk between ~20 and ~60 AU (the solid curve in Figure 13). For LkCa 15 (long dashed curve), Q is close to 1.5 between 60 and 160 AU while in all the other objects (short dashed curves) Q is well above the instability threshold. Since $Q \propto \Sigma(R)^{-1}$, it strongly depends on the assumed grain size distribution, as discussed in Section 6.1. In the case of the grain size model with $q = 3$ and variable $a_{\rm max}$, Q is always above 1.5 and GIs cannot occur. However, the smaller surface density leads to an higher ionization fraction, facilitating the role of the MRI. It seems therefore that both MRI or GI may be applicable in the observed objects.

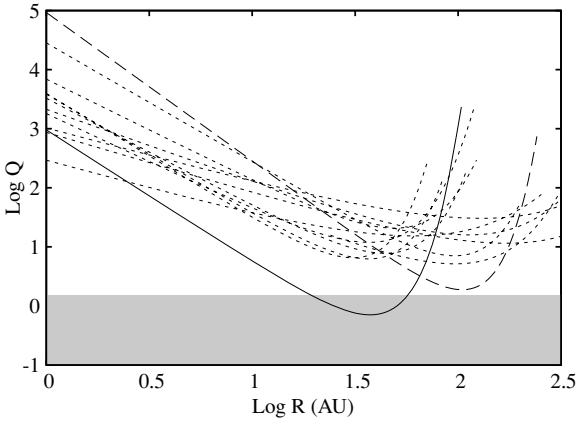

Figure 13. Radial profile of the GI parameters Q. The solid line corresponds to DG Tau, the long dashed line to LkCa 15, and the short dashed lines to other sources in the sample. The grey region ($Q < 1.5$) indicates where the disk is gravitationally unstable.

We compare the viscosity profile $\nu(R)$ from Equation (15) with the theoretical expectation of MRI and GI models by adopting the classical α viscous disk parameterization (Shakura & Sunyaev 1973) and writing the stress parameter α in the form (see Appendix E)

$$\alpha(R) \simeq \frac{3\times10^{-2}}{(2-\gamma)^2}\left(\frac{t_s}{1\ \rm Myr}\right)^{-1}\left(\frac{R_1}{10\ \rm AU}\right)^{(2-\gamma)} \times\left(\frac{R}{10\ \rm AU}\right)^{(\gamma-3/2)}\left(\frac{M_*}{0.5\ M_\odot}\right)^{1/2} T_i^{-1}(R). \quad (18)$$

It is of some importance to note that α is generally assumed to be constant in analytic modeling, although this choice has no physical justification and numerical simulations show variations of α both in space and time (Nelson & Papaloizou 2003). For a simple disk model that assumes $T_i(R) \propto R^{-1/2}$ (see Section 6), constant α corresponds to the case $\gamma = 1$. However, since the disk temperature T_i deviates from the $R^{-1/2}$ profile (Section 6.4) and we observe cases of $\gamma < 1$, α cannot be constant in the observed disks. Figure 14 shows the behavior of α for $\gamma > 0$ (upper panel), $\gamma \sim 0$ (middle panel), and $\gamma < 0$ (lower panel). In all cases, α decreases with the orbital radius R and it may vary by almost 4 orders of magnitude between 0.5 and 10^{-4}. For $\gamma > 0$, α has a shallow dependence on radius and ranges

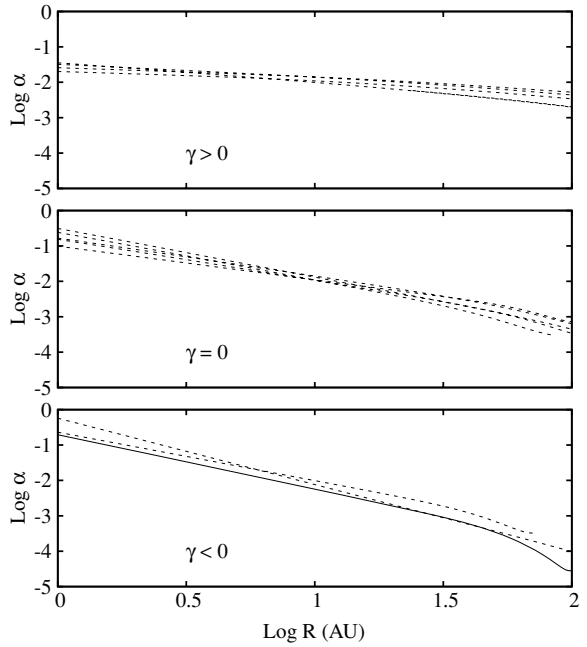

Figure 14. Derived values of the stress parameter α, for the observed circumstellar disks grouped according to $\gamma > 0$ (upper panel), $\gamma \sim 0$ (middle panel), and $\gamma < 0$ (lower panel).

from about 0.03, at 1 AU, to about 0.005, at 100 AU. For $\gamma \leqslant 0$, α varies more rapidly and assumes values larger than 0.1 inside radii of few AU and smaller than 0.001 outside about 30 AU.

Numerical simulations of a Keplerian disk affected by MRI suggest that α can range from 0.005 to 0.6 (see, e.g., the review of Balbus 2003). Although detailed comparison of the MRI model and our observations is beyond the scope of this work, we note that a decrement of α with the radius can be achieved for particular values of the magnetic field strength and geometry (Papaloizou & Nelson 2003). As discussed above, the DG Tau disk can be gravitationally unstable between 20 and 60 AU. In this region we calculate values of α between 0.001 and 0.003, which are slightly smaller than $\alpha \sim 0.05$ predicted by numerical simulation of gravitationally unstable disks (Lodato & Rice 2004).

Although our analysis is very qualitative, MRI seems to be able to account for the values of α derived in our sample disks, and, perhaps even the radial profiles. Nevertheless, it is still unclear whether circumstellar disks can be completely MRI active, or if the MRI is effective only in the very inner part of the disk (e.g., Chiang & Murray-Clay 2007). More importantly, it is still an open question why MRI would operate in different ways in our sample disks, leading to the variety of values of γ and α discussed above.

7.1.3. Implications for Parent Cores

Our viscous timescales and stellar ages suggest that the assumption $t \gg t_s$ made in Section 5.1 is probably not appropriate for the youngest objects, e.g., DG Tau, DR Tau, GSS 39, and SR 24 S. For these objects, with little time for disk expansion, the dust radial distribution should trace the initial disk structure resulting from the collapse of the parent core and provide insight into as yet unknown details of the formation process (e.g., André et al. 2008).

A simple relation between circumstellar disks and core properties can be obtained on the assumption that disks form from the collapse of rigidly rotating cores (Goodman et al. 1993; Shu et al. 1977). If ω_c is the core angular velocity and if the core angular momentum J is conserved during the collapse, the disk initial radius R_1 can be expressed as

$$R_1 \simeq 25 \left(\frac{\omega_c}{10^{-14}\ \mathrm{s}^{-1}}\right)^2 \left(\frac{M_*}{1\ M_\odot}\right)^3 \mathrm{AU} \qquad (19)$$

(Hueso & Guillot 2005; Dullemond et al. 2006). Here we have assumed that (1) the disk centrifugal radius R_c (i.e., the radius at which the angular momentum of the disk is equal to the angular momentum of the parent core) is similar to the radius that contains about 90% of the initial disk mass (i.e., $R_c \sim 2R_1$, Appendix C), (2) the disk mass is negligible compared to the mass of the central star, (3) the disk does not significantly expand while it is still accreting material from the envelope, (4) the temperature of the core is 10 K (Kirk 2007; Jijina 1999), and (5) the magnetic field does not play a significant role in the core collapse.

For our stellar masses (Table 1) and disk initial radii between 25 and 40 AU (Section 7.1), we derive core angular velocities between 5×10^{-15} and 2×10^{-14} s^{-1}. Assuming simple radial profiles of the core density, we can estimate the specific core angular momentum j (i.e., the angular momentum per mass unit $j = J/M$) required to form disks with initial radii in the observed range. We assume a core density gradient of $\rho(r) \propto r^{-2}$ and a core radius of 0.05 pc (Caselli et al. 2002, and references therein). The core specific angular momentum, $j = (2/9)\omega_c R_{\mathrm{core}}^2$, then lies between 8×10^{-5} and 4×10^{-4} km s^{-1} pc.

For dense core, specific angular momenta $j = (0.5 - 4) \times 10^{-3}$ km s^{-1} pc have been derived from the measurements of velocity gradients of chemical tracer such as NH_3 and N_2H^+, and for cores with masses in the range 1–10 $M_\odot$ (Goodman et al. 1993; Caselli et al. 2002). These values are an order of magnitude larger than required to form disks with initial radii between 25 and 40 AU, suggesting that about 10% of the specific core angular momentum and about 30% of the core mass are conserved during the disk formation.

7.2. Interpreting "Transitional" Disks

The surface density in disks with $\gamma < 0$ (i.e., LkCa15, TW Hya, and DG Tau) increases with the orbital radius and reaches a maximum at $R \sim R_t$ (Section 6). This effect can mimic the inner disk clearing advocated to explain the deficit in the near- and mid-infrared excess over the stellar photosphere observed in "transitional" disks (Strom et al. 1989) where, it is postulated, planetary system formation may have begun (Espaillat et al. 2008). Thus, for LkCa 15 and TW Hya, we predict a gradual decrease of the surface density inside radii of ~60 and ~17 AU respectively, in qualitative agreement with the radii of the dust depleted disk region already inferred from mm-wave observations (Piétu et al. 2006; Hughes et al. 2007).

Figure 15 shows the observed SED of LkCa 15 (points) and the disk model of Table 5 that fits our 1.3 mm observations (solid line). The disk surface density is characterized by $\gamma = -0.8$ and extends up to the disk inner radius without any discontinuity (see Figure 7(a)). At about $R = 0.1$ AU, the dust sublimates, forming a "puffed-up" inner rim (Isella & Natta 2005) which emits mostly in the near-infrared between 1 and 3 μm (long-short dashed lines). For $R > 0.1$ AU, the optically thin disk surface layer emits in the mid- and far-infrared (short-dashed line) while the colder disk midplane dominates the emission at longer wavelengths (long-dashed line). The model reproduces well the observed SED.

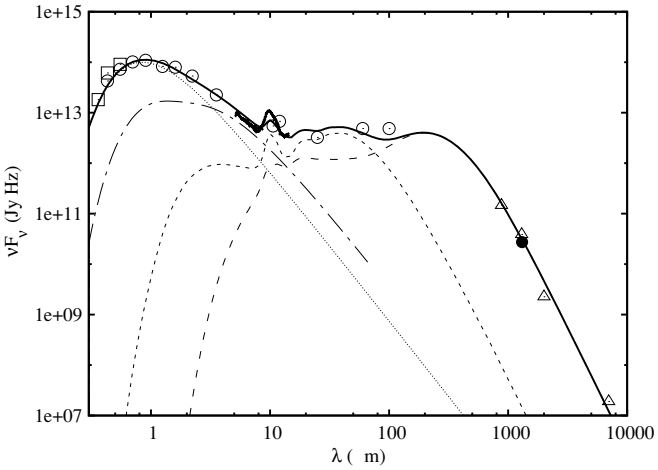

Figure 15. SED of LkCa15. Flux measurements from 2MASS, Kenyon & Hartmann (1995), Kitamura et al. (2002), Rodmann et al. (2006), Andrews et al. (2007) are represented by open squares, open circles and open triangles respectively. Our CARMA data are shown as filled circle, while data between 5 and 14 μm are from the Spitzer IRS archive. The solid line is the SED for the disk model that fits our CARMA 1.3 mm continuum observations (Table 5). This comprises the stellar photosphere (dotted line), a "puffed-up" inner rim (long-short dashed line), a disk surface layer (short dashed line), and a disk midplane (short dashed line).

Until now, photoevaporation, the presence of a planet, grain growth, and inside-out MRI clearing have been the main processes invoked to explain the properties of transitional disks (Alexander et al. 2006; Calvet 2005; Espaillat et al. 2008; Dullemond & Dominik 2005; Chiang & Murray-Clay 2007). Here we suggest disk viscosity as an additional means of producing a surface density profile and SED consistent with this class of disks. In fact, the similarity solution for the disk surface density predicts partially depleted inner disks whenever the viscosity $\nu(R) \propto R^{\gamma}$ decreases with the orbital radius.

If transitional disks are explained by the similarity solution for the disk surface density, the surface densities at $R < R_t$ and $R > R_t$ are then tightly correlated by Equation (9). In particular, since γ must be negative, the surface density must fall off very quickly for $R > R_t$ (see Figure 4). The outer disk in transitional objects must be therefore characterized by a rapid decrease of the surface brightness measured at millimeter wavelengths. In our sample this hold true for LkCa15 and TW Hya but it is not verified for DM Tau and GM Aur. For the latter two objects, the observed dust continuum emission at $R \gtrsim 45$ AU leads to positive value of γ, implying that the surface density in DM Tau and GM Aur increases smoothly up to the inner disk radius (see Figure 7). This contrasts with the observations of dust depleted inner disks within about 7 and 20 AU (Calvet 2005).

We suggest that this interpretation of "transitional disks" is applicable when the dust-depleted inner region occupies a significant fraction of the disk extent. In LkCa15 and TW Hya, R_t is in fact more than 20% of the disk radius R_d (Table 5). By contrast, when the dust-depleted inner region is only a few percent of the disk radius, as for DM Tau and GM Aur, the presence of a planet, the inside-out MRI clearing, or the photoevaporation by the central star are more probable explanations for the inner disk clearing.

7.3. Similarity with the Solar Nebula

A fundamental question regarding pre-main-sequence disks is whether they will evolve into planetary systems similar to our own. Addressing this question is difficult mainly because we have a limited knowledge on the properties of the solar nebula. A recent re-analysis of the distribution of solid bodies in the solar system by Davis (2005) differs from earlier studies (Kusaka 1970; Weidenschilling 1977; Hayashi 1981) and suggests that the surface density distribution in the solar nebula at 10^5–10^6 yr from its formation is described by

$$\Sigma(R) \simeq 1.14 \times 10^3 R^{-1/2} e^{-0.024 R^{3/2}}. \quad (20)$$

The numerical constants are chosen to recover the total mass of the solar nebula, 0.02 $M_{\odot}$ (Kusaka 1970), and its specific angular momentum $j = 8.7 \times 10^{-6}$ km s^{-1} pc (Cox 2000).

The solar nebula surface density of Equation (20) is based on the assumption that $\gamma = 0.5$, and corresponds to the similarity solution expressed by Equation (9) for $R_t = 6$ AU and $\Sigma_t = 340$ g cm^{-2}. The total mass for the solar nebula are quite similar to the values measured for GSS 39, GM Aur, DM Tau, and GO Tau. However, the solar nebula transition radius, R_t, is at least a factor of 4 smaller than what found for objects with ages of 10^5–10^6 yr (see Sections 6.2 and 7.1.3).

Indeed, among our disk sample, only TW Hya may be a good match to the solar nebula, being the only old object characterized by a small transition radius. If TW Hya underwent viscous evolution similar to that discussed in Section 7.1, it probably formed with an initial transition radius of 4–8 AU, similar to that predicted for the solar nebula.

8. CONCLUSIONS

We presented high angular resolution (0.″7) interferometric observations of the 1.3 mm continuum emission from 14 pre-main-sequence circumstellar disks. The disk surface brightness is characterized by a range of radial profiles. Adopting the similarity solution for disk surface density (Hartmann et al. 1998) and a self consistent disk emission model (Isella et al. 2007), we derived for each disk a surface density radial profile defined by the transition radius R_t, the surface density Σ_t and the slope of the disk viscosity γ, as well as a radial temperature profile and its orientation in space. Assuming a constant dust opacity throughout the disk, we find that the different surface brightness profiles are mainly due to differences in R_t and γ, which in turn imply different disk surface densities.

From a comparison of the disk surface density and the stellar properties, it appears that the disk transition radius R_t is correlated with the stellar age and increases from ∼20 to ∼100 AU over about 3–5 Myr. This disk expansion appears to be accompanied by a decrease in the mass accretion rate. We argue that these temporal variations of the disk radius and the mass accretion rate support a scenario in which disks form an evolutionary sequence. The observed evolution is in qualitative agreement with that of viscous disk models if the initial disk masses are between 0.05 and 0.4 $M_{\odot}$ and the initial radii R_1 range from 20 to 45 AU. Note, however, that disk masses can vary by one order of magnitude depending on the assumed dust opacity. The temporal variation of the disk radius and mass constrains the viscous timescale t_s at the disk initial radius R_1 to be between 0.1 to 0.3 Myr.

The viscous disk model assumes that the disk viscosity $\nu(R)$ scales as R^{γ}. Among our sample, γ ranges from −0.8 to 0.8, leading to a large variety of viscosity radial profiles. Parameterizing the disk viscosity in terms of the stress parameter α, we show that α scales with radius R roughly as $R^{\gamma-1}$. Since γ is always smaller than 1, α must decrease with the orbital radius.

We suggest that α may vary by almost 4 orders of magnitude between 0.5 and 10^{-4}. These values are in general agreement with MRI models, which is probably the main source of viscosity at the surface densities of our disks. However, its still an open question why MRI should operate differently among our sample, leading to a large range of values of γ.

The ages of the younger stars in our sample are comparable to the viscous timescale of 0.1–0.3 Myr. It seems likely that, with little time for the disk expansion, the dust radial distribution should trace the initial disk structure resulting from the collapse of the parent core. For typical assumptions on the core rotation, radial density profile, and radius, we derive the core specific angular momentum $j = J/M$ required to form disks with initial radii between 20 and 45 AU. We argue that j must range from 8×10^{-5} to 4×10^{-4} km s^{-1} pc, and suggest that this corresponds to about 10% of the specific angular momentum measured in dense cores. It seems therefore likely that during the star formation process, about 10% of the core angular momentum is transferred to the circumstellar disk. Alternatively, 10% efficiency in conserving angular momentum implies that about 30% of the core mass is used to form the central star. We believe that the attempt to correlate the properties of circumstellar disks and dense cores, though still very qualitative, is an important step forward to understand the role of disks in conserving the angular momentum during the star formation process. Clearly, the capability to investigate this aspect in detail is actually hampered by the sensitivity and resolution of the existing interferometers, which limit the analysis to a few bright objects. However, the ongoing improvement of facilities such as CARMA and VLA, and the advent of ALMA, will enable us to expand the number of spatially resolved disks by a large factor and have a more complete view on the relations between dense core and young disks.

We point out that in disks with $\gamma < 0$, the surface density $\Sigma(R)$ increases with radius R and reach a maximum at about the transitional radius R_t. We argue that this particular behavior of $\Sigma(R)$ can mimic the inner disk clearing advocated to explain the dominant characteristic of some "transitional disks," namely a deficit in the near- and mid-infrared excess over the stellar photosphere and the presence of an "hole" in the surface brightness observed at millimeter wavelengths. For LkCa15, we show that a surface density with $\gamma = -0.8$ that extends without any discontinuity up to the disk inner radius located at few stellar radii can reproduce both the SED and the 1.3 mm continuum emission. By contrast, we find no clear explanation in terms of the similarity solution of the surface density for the dust depleted inner disks around DM Tau and GM Aur. It seems likely that "transitional disks" may originate from a large variety of effects.

Finally, it appears that most of the disks in our sample are very different from the currently accepted view of the solar nebula. While most of them have masses similar to the minimum mass solar nebula, 0.02 $M_\odot$, their transitional radii are at least a factor 4 larger than the value $R_t \sim 6$ AU derived from the actual distribution of solid bodies in the solar system (Davis 2005). The exception is TW Hya which has a very small disk radius, $R_t \sim 17$ AU, compared to its large age, $t = 7$ Myr. We argue that TW Hya disks probably formed with R_t in the range from 4 to 8 AU, and may well reflect the properties of our early solar system.

We are indebted to Meredith Hughes and David Wilner for providing the SMA data of GM Aur and TW Hya. We thank Antonella Natta, Sean Andrews, and Leonardo Testi for the useful discussions and the referee for the very useful comments. We thank the OVRO/CARMA staff and the CARMA observers for their assistance in obtaining the data. We acknowledge support from the Owens Valley Radio Observatory, which is supported by the National Science Foundation through grant AST 05-40399. This work was performed in part under contract with the Jet Propulsion Laboratory (JPL) funded by NASA through the Michelson Fellowship Program. JPL is managed for NASA by the California Institute of Technology.

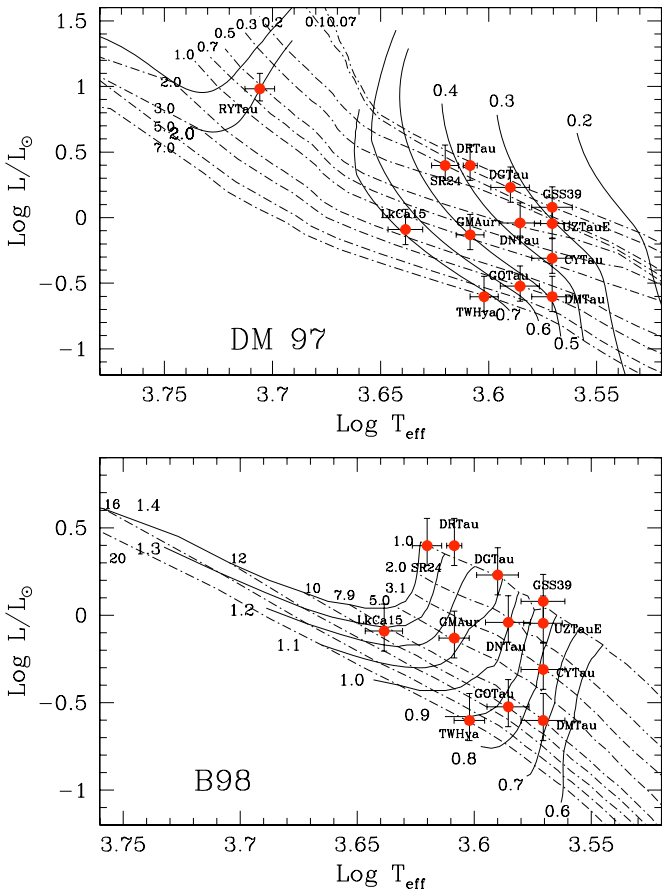

Figure 16. Position on the H–R diagram of the observed sources. The upper panel show the theoretical models by D'Antona & Mazzitelli (1997) while the lower panel the models of Baraffe et al. (1998). The dashed lines correspond to the stellar isocrones for ages in Myr as labeled at the left end of the lines while the solid lines correspond to the stellar evolution sequence for stellar masses between 0.2 and 1.7 $M_\odot$ as labeled at the lower end of the lines.

(A color version of this figure is available in the online journal.)

APPENDIX A

STELLAR AGES AND MASSES

Figure 16 shows the location of our sample stars in the H–R diagram with the evolutionary models of D'Antona & Mazzitelli (1997, hereafter DM97) and Baraffe et al. (1998, B98). The uncertainties on the stellar temperature correspond to half a spectral type, while the stellar luminosity is uncertain by 30%. From DM97 models, the stellar ages range from 0.1 Myr (DR Tau and DG Tau) to 7 Myr (TW Hya). In Taurus-Auriga alone the age spread is 1–3 Myr. However, as illustrated in the upper panel of Figure 17, these ages are smaller than those inferred from B98 by factor of 2.6-10. Similarly, the lower panel of Figure 17 shows that the stellar masses inferred from B98 are

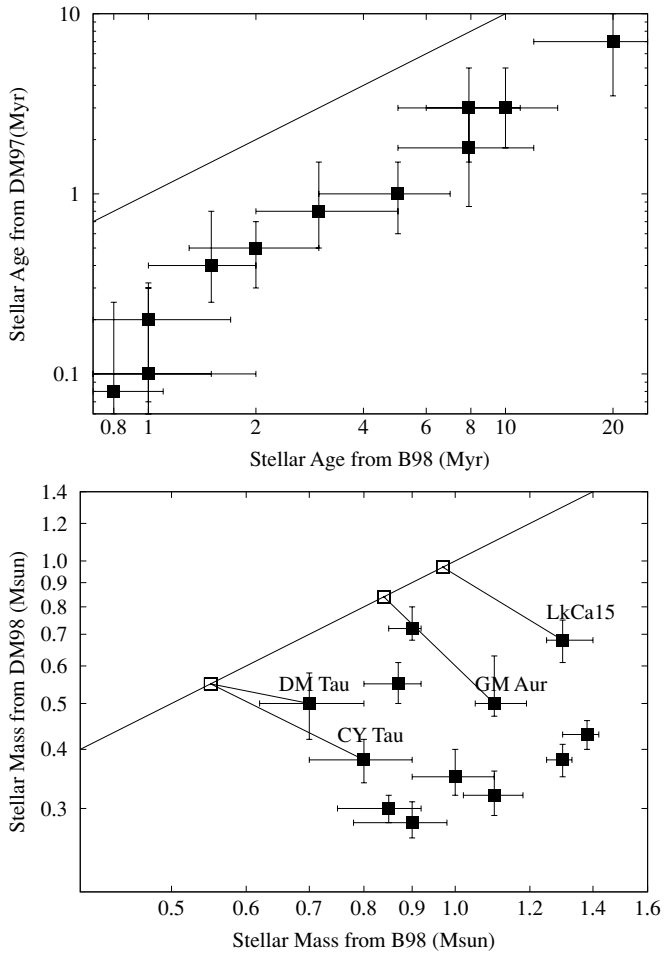

Figure 17. Upper panel: stellar ages derived from DM97 versus the ages derived from the B98 models. The solid lines correspond to equal ages. The comparison between stellar masses is shows in the lower panel. The open squares identify the dynamical stellar masses derived by Simon et al. (2000) for DM Tau, CY Tau, GM Aur, and LkCa 15

systematically larger than those from DM97 by factors of 1.2–3.4. Neither model reproduces the dynamical masses derived by Simon et al. (2000) for DM Tau, GM Aur, CY Tau, and LkCa 15. Typically the DM97-derived masses are lower than the dynamical masses by 10%–40% while B98-masses are lower by 20%–30%. For the purpose of our analysis we have adopted DM97 models because they enable us to derive masses and ages for all the stars in our sample, while RY Tau and MWC 275 are outside the temperature and luminosity range of the BH98 model.

APPENDIX B

FITTING PROCESS

For fixed stellar parameters, dust opacity, and disk inner radius, the dust emission model is defined by the state $\boldsymbol{x}\{i, \mathrm{P.A.}, R_t, \Sigma_t, \gamma\}$, where i is the disk inclination, P.A. is the disk position angle measured from north to east, R_t is the disk transition radius, Σ_t is the disk surface density at R_t and γ defines the shape of the disk surface density, as discussed in Section 5.1. The model that best fits the observations is found through the minimization of χ^2 (Equation (2)). We adopt a Bayesian approach in which the joint probabilities for the observed data d and the given model state x are described as the product of the probability of the observed data $\boldsymbol{d}$ given the model parameters $\boldsymbol{x}$ (i.e., the likelihood), and a known prior probability distribution function $p(\boldsymbol{x})$ of the model parameters:

$$p(\boldsymbol{x}|\boldsymbol{d}) \propto p(\boldsymbol{x})p(\boldsymbol{d}|\boldsymbol{x}). \quad \text{(B1)}$$

In this framework, the best-fit model corresponds to the state $\boldsymbol{x}$ that maximizes the a posteriori distribution $p(\boldsymbol{x}|\boldsymbol{d})$.

To characterize the posteriori distribution we adopt a Markov Chain Monte Carlo (MCMC) method (see, e.g., Ford 2005; Fitzgerald et al. 2007). This method generates a chain of states $\boldsymbol{x}$ sampled from a desired probability function $p(\boldsymbol{x})$, whose equilibrium distribution is equal to the posteriori distribution $p(\boldsymbol{x}|\boldsymbol{d})$. In our specific case, since complex visibilities errors are described by a normal distribution (Wrobel & Walker 1999), the probability of the observables (i.e., the real and imaginary part of the complex visibility) given the model state $\boldsymbol{x}$ is expressed by the χ^2 distribution. To a first approximation this is proportional to $e^{-\chi^2(\boldsymbol{x})/2}$. In the most general case, where all model states have the same prior probability and $p(\boldsymbol{x}) \sim 1$, the posteriori joint probability is also roughly proportional to $e^{-\chi^2(\boldsymbol{x})/2}$. The state that maximizes $p(\boldsymbol{x}|\boldsymbol{d})$ therefore correspond to the state that minimizes $\chi^2(\boldsymbol{x})$, justifying the choice of the χ^2 as the maximum likelihood estimator.

The MCMC fitting is realized following Ford (2005) and is briefly summarized here. First, the chain is constructed using the Metropolis-Hastings algorithm with the Gibbs sampler, and generating a chain of models where the $(n+1)$th state depends only on the n-th state through a specified transition probability $q(n|n+1)$. In practice, at each nth step of the chain we (1) generate a random trail state $\boldsymbol{x}'$ adopting a transition probability described by a Gaussian distribution centered on $\boldsymbol{x}$, (2) calculate $\chi^2(\boldsymbol{x}')$, and (3) accept the trail state as the new $(n+1)$th state of the chain if it satisfies an acceptance probability $\alpha(\boldsymbol{x}'|\boldsymbol{x}_n)$ specified by the M-H algorithm, namely if

$$\alpha(\boldsymbol{x}'|\boldsymbol{x}_n) = \min\left\{-\frac{1}{2}[\chi^2(\boldsymbol{x}') - \chi^2(\boldsymbol{x}_n)], 1\right\} \geqslant u \quad \text{(B2)}$$

where u is a random number generated from a uniform distribution between 0 and 1. For the Gibbs sampler, the trial state $\boldsymbol{x}'$ is generated by substituting only a subset of parameters from the state $\boldsymbol{x}$. In particular, since R_t, Σ_t and γ are correlated (Equation (9)), we choose to change these three parameters at the same time, while varying the inclination and the position angle independently. At each step, the parameter(s) to be updated (x_μ) are then randomly modified with a transition probability of

$$q(x'_\mu|x_\mu) = \frac{1}{\sqrt{2\pi\beta_\mu^2}} \exp\left[-\frac{(x'_\mu - x_\mu)^2}{2\beta_\mu^2}\right], \quad \text{(B3)}$$

where the variance β_μ defines the variability interval for each parameter. The model fitting results depend neither on the choice of the transition probability $q(\boldsymbol{x}'|\boldsymbol{x})$ nor on how the Gibbs sampler is implemented. However, these strongly affect the efficiency of the model fitting and must be carefully chosen to allow a fast convergence toward the equilibrium distribution. Here, each parameter is allowed to vary over a large interval and the variance β_μ is chosen so that the overall acceptance rate is close to the optimal value of ~0.25 (Gelman et al. 2003).

To select the initial state of the chain we adopt two different approaches. First, the initial parameters for the disk are set based on the Gaussian fit to the observations (Table 3); the

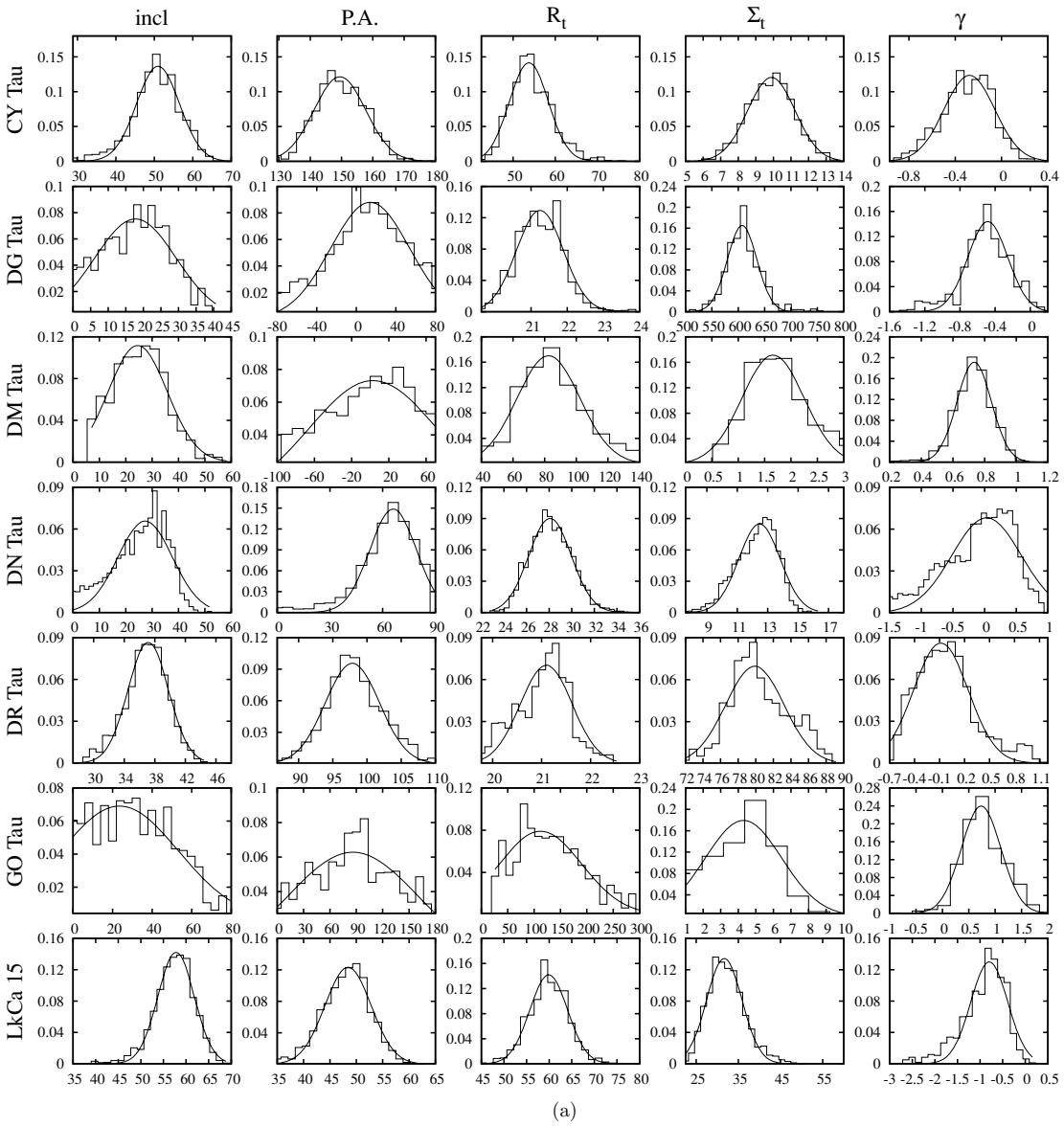

(a)

Figure 18. Normalized probability distributions for the disk inclination (°), P.A. (°), transition radius R_t (AU), surface density Σ_t (g cm^{-2}) and γ obtained from the MCMC fitting process, as discussed in Appendix B. The solid line corresponds to the best-fit Gaussian distribution used to derive the parameter uncertainties reported in Table 5

initial inclination and P.A. are calculated from the aspect ratio of the emission, the transition radius R_t is assumed to be the half width along the major axis at half maximum, p is set to be 0.5, and Σ_t is randomly chosen between 0.1 and 1000 g cm^{-2}. This choice is usually close to what provided by the best-fit model and enables a quick convergence of the chain. Unfortunately, like most algorithms developed to minimize the χ^2, the MCMC can be trapped in local minima if they are separated by sufficiently high χ^2 barriers. To compensate, additional randomly initialized MCMC chains were run to verify that they all converge to the same final state.

Once the equilibrium distribution of the MCMC chain is sufficiently well sampled—usually requiring a run of a minimum of 10^4 models—the distribution of each parameter is obtained through marginalization, i.e., by integrating the posteriori distribution (now equivalent to the MCMC equilibrium distribution) over all the parameters except the one in which we are interested. We show in Figure 18 the obtained posteriori distributions for the model parameters. These are generally consistent with a normal profile, supporting our decision to adopt a Gaussian transition probability $q(\boldsymbol{x}'|\boldsymbol{x})$, and enables expressing the parameter uncertainties in terms of the standard deviation σ of the probability distribution.

APPENDIX C

CUMULATIVE AND TOTAL DISK MASS

We integrate the surface density (Equation (9)) to derive the cumulative disk mass, i.e., the disk mass contained within a radius R at time t. Since $R_{\rm in} \ll R_t$ we obtain

$$M_d(R,t) = 4\pi\Sigma_t R_t^2 e^{1/2(2-\gamma)} \times \left\{1 - \exp\left[-\frac{1}{2(2-\gamma)}\left(\frac{R}{R_t}\right)^{(2-\gamma)}\right]\right\}. \quad \text{(C1)}$$

The total disk mass at the time t is therefore obtained for $R \to \infty$ in the form

$$M_d(t) = 4\pi\Sigma_t R_t^2 e^{1/2(2-\gamma)}. \quad \text{(C2)}$$

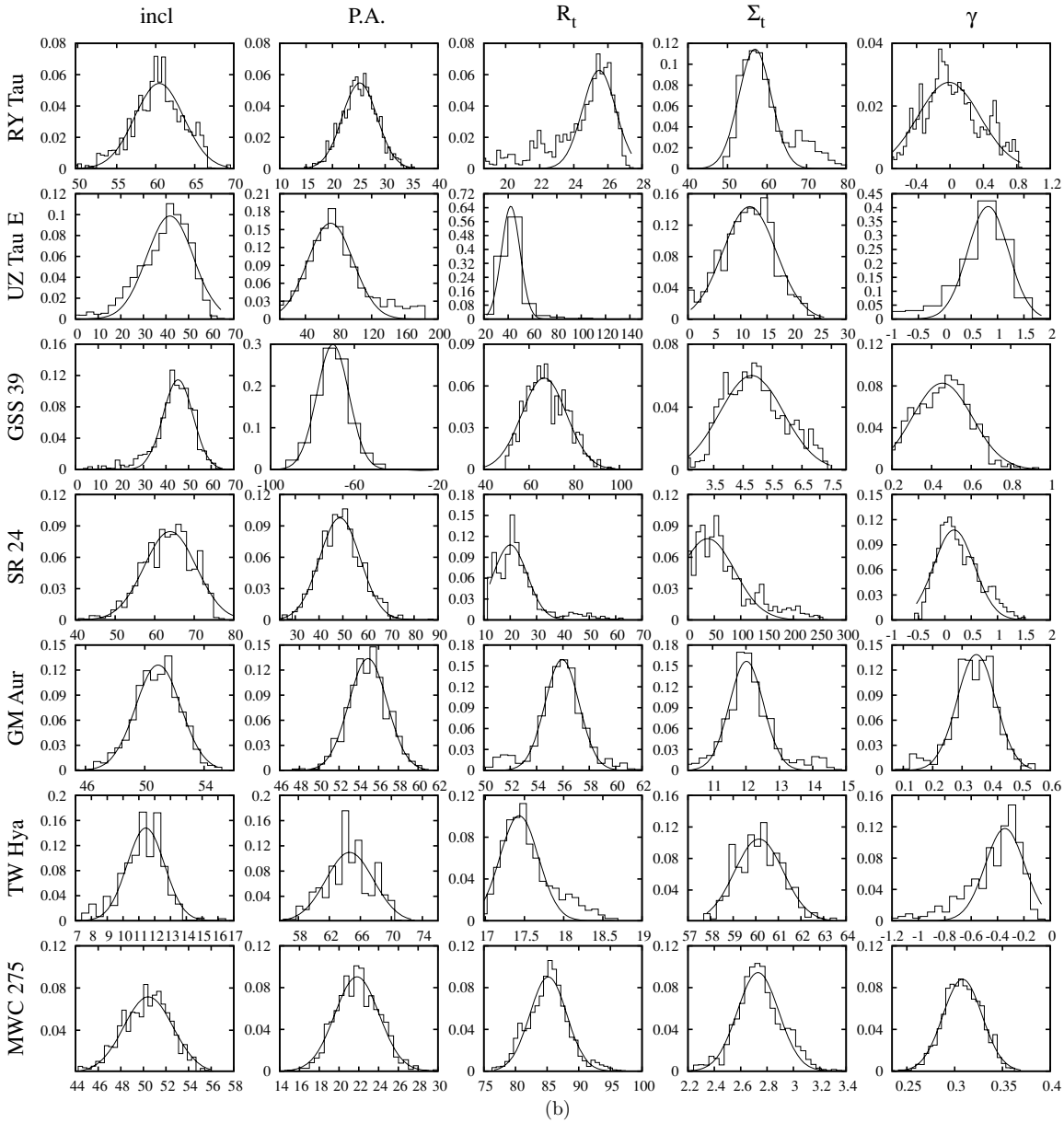

(b)

Figure 18. (Continued)

Using the last two equations we derive that the disk mass contained inside the transition radius R_t is 39% of the total disk mass if $\gamma = 1$ and 22% if $\gamma = 0$.

Using Equation (C1) and Equation (C2) we can also demonstrate that R_1 is the radius containing ∼63% of the initial disk mass $M_d(t = 0)$. We can write

$$\frac{M_d(R_1, 0)}{M_d(0)} = 1 - \exp\left[-\frac{1}{2(2-\gamma)}\left(\frac{R_1}{R_{t,0}}\right)^{(2-\gamma)}\right] \quad \text{(C3)}$$

where the transitional radius at $t = 0$, given by Equation (8), is

$$R_{t,0} = R_1\left[\frac{1}{2(2-\gamma)}\right]^{1/(2-\gamma)}. \quad \text{(C4)}$$

Substituting this latter equations in Equation (C3), we obtain

$$\frac{M_d(R_1, 0)}{M_d(0)} = 1 - e^{-1} \simeq 0.63 \quad \text{(C5)}$$

We finally calculate that about 90% of the initial disk mass is contained within $2R_1$. From Equations (C3) and (C4) we can write

$$\frac{M_d(2R_1, 0)}{M_d(0)} = 1 - e^{-2^{(2-\gamma)}} \quad \text{(C6)}$$

which is equal to 0.86 for $\gamma = 1$ and 0.98 for $\gamma = 0$.

APPENDIX D

MASS ACCRETION RATE ON THE CENTRAL STAR

From Equations (5) and (9) the surface density Σ_t at the transition radius R_t can be expressed as

$$\Sigma_t = \frac{C}{3\pi\nu_1}\tilde{t}^{-(5/2-\gamma)/(2-\gamma)}\left(\frac{R_1}{R_t}\right)^{\gamma} \times \exp\left[-\frac{1}{2(2-\gamma)}\right]. \quad \text{(D1)}$$

Writing the initial disk mass $M_d(0)$ in the form

$$M_d(0) = \frac{2}{3}\frac{C}{\nu_1}\frac{R_1^2}{2-\gamma}, \tag{D2}$$

we can eliminate the ratio C/ν_1 from Equation (D1) to obtain

$$\Sigma_t = \frac{M_d(0)}{4\pi R_t^2}\tilde{t}^{-1/2(2-\gamma)}e^{-1/2(2-\gamma)}. \tag{D3}$$

Substituting the definition of R_t from Equation (8), Σ_t takes the form

$$\Sigma_t \propto \frac{M_d(0)}{4\pi R_1^2}\tilde{t}^{-5/(2(2-\gamma))}. \tag{D4}$$

Starting from the expression of the mass flow (Hartmann et al. 1998)

$$\dot{M}(r,t) = C\tilde{t}^{-\frac{(5/2-\gamma)}{(2-\gamma)}}\exp\left[-\frac{r^{(2-\gamma)}}{\tilde{t}}\right]\times\left[1-\frac{2(2-\gamma)r^{(2-\gamma)}}{\tilde{t}}\right] \tag{D5}$$

and substituting the expression for the constant C derived from Equation (D2), we can express the mass flow as

$$\dot{M}(R,t) = \frac{M_d(0)}{2(2-\gamma)t_s}\left[1-\left(\frac{R}{R_t}\right)^{(2-\gamma)}\right]\tilde{t}^{-(5/2-\gamma)/(2-\gamma)} \exp\left[-\frac{R^{(2-\gamma)}}{2(2-\gamma)R_t^{2-\gamma}}\right], \tag{D6}$$

where t_s is the viscous timescale defined by the Equation (6) and

$$r = \frac{R}{R_1} = \frac{R}{R_t}\frac{R_t}{R_1} = \frac{R}{R_t}\left[\frac{\tilde{t}}{2(2-\gamma)}\right]^{1/(2-\gamma)}. \tag{D7}$$

Note that for $\gamma = 1$, Equation (D6) reduces to Equation (35) in Hartmann et al. (1998).

At radii smaller than the transitional radius R_t, the material within the disk moves inward and finally falls onto the central star. The mass accretion rate $\dot{M}_{\rm acc}(t)$ is given by Equation (D6) with R equal to the radius at which the disk is truncated by the accretion process. Since this radius is of the order of a fraction of AU and much smaller than the transitional radius R_t, $\dot{M}_{\rm acc}$ takes the form

$$\dot{M}_{\rm acc}(t) = \frac{M_d(0)}{2(2-\gamma)t_s}\tilde{t}^{-(5/2-\gamma)/(2-\gamma)}. \tag{D8}$$

APPENDIX E

DERIVATION OF α IN THE CASE $\gamma \neq 1$

In this section we derive the value of α for the similarity solution of the disk surface density in the general case $\gamma \neq 1$. We adopt the classical α parameterization of the disk viscosity in the form (Shakura & Sunyaev 1973)

$$\nu = \alpha c_s H. \tag{E1}$$

If the disk is in keplerian rotation, vertically isothermal and in hydrostatic equilibrium (see the discussion in Section 5.2), the sound speed is given by

$$c_s = H\cdot\Omega = H\cdot\sqrt{GM_*/R^3} \tag{E2}$$

with

$$H = R^{3/2}\sqrt{\frac{k_bT_i(R)}{\mu m_H G M_*}}, \tag{E3}$$

where k_b is Boltzman's constant, $\mu = 2.33$ g mol^{-1} (Ruden & Pollack 1991) is the mean molecular weight of the circumstellar material, m_H is the proton mass, G is the gravitational constant, and $T_i(R)$ is the disk interior temperature. Substituting Equation (E2) and E3 in Equation (E1), we can express the disk viscosity as a function of the radius in the form

$$\nu(R) = \frac{k_b}{\mu m_H\sqrt{GM_*}}\cdot\alpha R^{3/2}T_i(R). \tag{E4}$$

Comparison of Equation (15) and Equation (E4) provides, therefore, an expression of α in the form

$$\alpha(R) \simeq \frac{3\times10^{-2}}{(2-\gamma)^2}\left(\frac{t_s}{1\ \rm Myr}\right)^{-1}\left(\frac{R_1}{10\ \rm AU}\right)^{(2-\gamma)} \times\left(\frac{R}{10\ \rm AU}\right)^{(\gamma-3/2)}\left(\frac{M_*}{0.5\ M_\odot}\right)^{1/2}T_i^{-1}(R). \tag{E5}$$

REFERENCES

Alexander, R. D., Clarke, C. J., & Pringle, J. E. 2006, MNRAS, 369, 216
André, P., Basu, S., & Inutsuka, S. 2008, in Structure Formation in Astrophysics, ed. G. Chabrier (Cambridge: Cambridge Univ. Press), 254
Andrews, S. M., & Williams, J. P. 2005, ApJ, 631, 1134
Andrews, S. M., & Williams, J. P. 2007, ApJ, 659, 705
Balbus, S. A. 2003, ARA&A, 41, 555
Balbus, S. A., & Hawley, J. F. 1991, ApJ, 376, 214
Balbus, S. A., & Hawley, J. F. 2000, SSRv, 92, 39
Baraffe, I., Chabrier, G., Allard, F., & Hauschildt, P. H. 1998, A&A, 337, 403
Bechwith, S. V. W., & Sargent, A. I. 1991, ApJ, 381, 250
Brauer, F., Dullemond, C. P., & Henning, Th. 2008, A&A, 480, 859
Brown, J. M., Blake, G. A., Qi, C., Dullemond, C. P., & Wilner, D. J. 2008, ApJ, 675, 109
Calvet, N., & Gullbring, E. 1998, ApJ, 509, 802
Calvet, N., et al. 2005, ApJ, 630, 185
Caselli, P., Benson, P. J., Myers, P. C., & Tafalla, M. 2002, ApJ, 572, 238
Chiang, E. I., & Goldreich, P. 1997, ApJ, 490, 368
Chiang, E. I., Joung, M. K., Creech-Eakman, M. J., Qi, C., Kessler, J. E., Blake, G. A., & van Dishoeck, E. F. 2001, ApJ, 547, 1077
Chiang, E. I., & Murray-Clay, R. A. 2007, Nat. Phys., 3, 604
Cox, A. N. 2000, Allen's Astrophysical Quantities (4th ed.; New York: Springer)
D'Antona, C., Caloi, F., & Mazzitelli, I. 1997, ApJ, 477, 519
Davis, S. S. 2005, ApJ, 627, 153
Dullemond, C. P., & Dominik, C. 2005, A&A, 434, 971
Dullemond, C. P., Dominik, C., & Natta, A. 2001, ApJ, 560, 957
Dullemond, C. P., Natta, A., & Testi, L. 2006, ApJ, 645, 69
Dutrey, A., Guilloteau, S., Duvert, G., Prato, L., Simon, M., Schuster, K., & Menard, F. 1996, A&A, 309, 493
Dutrey, A., Guilloteau, S., & Guelin, M. 1997, A&A, 317, 55
Espaillat, C., Calvet, N., Luhman, K. L., Muzerolle, J., & D'Alessio, P. 2008, ApJ, 682, L125
Fitzgerald, M. P., Kalas, P. G., & Graham, J. R. 2007, ApJ, 670, 557
Ford, Eric B. 2005, AJ, 129, 1706
Furlan, E., et al. 2006, ApJS, 165, 568
Garcia Lopez, R., Natta, A., Testi, L., & Habart, E. 2006, A&A, 459, 837
Gelman, A., Carlin, J. B., Stern, H. S., & Rubin, D. B. 2003, Bayesian Data Analysis (2nd ed.; Boca Raton, FL: Chapman & Hall/CRC)
Goodman, A. A., Benson, P. J., Fuller, G. A., & Myers, P. C. 1993, ApJ, 406, 528
Guilloteau, S., Dutrey, A., & Simon, M. 1999, A&A, 348, 570
Hartmann, L., Calvet, N., Gullbring, E., & D'Alessio, P. 1998, ApJ, 495, 385
Hayashi, T. 1981, Prog. Theor. Phys. Suppl., 70, 35
Hernández, J., et al. 2007, ApJ, 662, 1067
Hueso, R., & Guillot, T. 2005, A&A, 442, 703
Hughes, A. M., Wilner, D. J., Calvet, N., D'Alessio, P., Claussen, M. J., & Hogerheijde, M. R. 2007, ApJ, 664, 536

Hughes, A. M., Wilner, D. J., Qi, C., & Hogerheijde, M. R. 2008, ApJ, 678, 1119
Jensen, E. L. N., Koerner, D. W., & Mathieu, R. D. 1996, AJ, 111, 2431
Jijina, J., Myers, P. C., & Adams, Fred, C., ApJS, 125, 161
Kenyon, S., & Hartmann, L. 1995, ApJS, 101, 117
Kirk, H., Johnstone, D., & Tafalla, Ma. 2007, ApJ, 668, 1042
Kitamura, Y., Momose, M., Yokogawa, S., Kawabe, R., Tamura, M., & Ida, S. 2002, ApJ, 581, 357
Kusaka, T., Nakano, T., & Hayashi, C. 1970, Prog. Theo. Phys., 44, 1580
Isella, A., & Natta, A. 2005, A&A, 438, 899
Isella, A., Testi, L., & Natta, A. 2006, A&A, 451, 951
Isella, A., Testi, L., Natta, A., Neri, R., Wilner, D., & Qi, C. 2007, A&A, 469, 213
Lynden-Bell, D., & Pringle, J. E. 1974, MNRAS, 168, 603
Lodato, G., & Rice, W. K. M. 2004, MNRAS, 351, 630
Muzerolle, J., Calvet, N., Briceño, C., Hartmann, L., & Hillenbrand, L. 2000, ApJ, 535, 47
Muzerolle, J., Calvet, N., & Hartmann, L. 1998, ApJ, 492, 743
Natta, A., Testi, L., & Randich, S. 2006, A&A, 452, 245
Natta, A., Testi, L., Calvet, N., Henning, Th., Waters, R., & Wilner, D. 2007, in Protostars and Planets V, ed. B. Reipurth, D. Jewitt, & K. Keil (Tucson, AZ: Univ. of Arizona Press), 767
Nelson, R. P., & Papaloizou, J. C. B. 2003, MNRAS, 339, 993
Papaloizou, J. C. B., & Nelson, R. P. 2003, MNRAS, 339, 983
Patience, J., Akeson, R. L., & Jensen, E. L. N. 2008, ApJ, 677, 616
Piétu, V., Dutrey, A., & Guilloteau, S. 2007, A&A, 467, 163
Piétu, V., Dutrey, A., Guilloteau, S., Chapillon, E., & Pety, J. 2006, A&A, 460, 43
Piétu, V., Guilloteau, S., & Dutrey, A. 2005, A&A, 443, 945
Pollack, J. B., Hollenbach, D., Beckwith, S., Simonelli, D. P., Roush, T., & Fong, W. 1994, ApJ, 421, 615
Press, W. H., Teukolsky, S. A., Vetterling, W. T., & Flannery, B. P. 2007, Numerical Recipes (Cambridge: Cambridge Univ. Press)
Pringle, J. E. 1981, ARA&A, 19, 137
Qi, C., et al. 2004, ApJ, 616, 11
Rebull, L. M., Wolff, S. C., & Strom, S. E. 2004, AJ, 127, 1029
Rodmann, J., Henning, Th., Chandler, C. J., Mundy, L. G., & Wilner, D. J. 2006, A&A, 446, 221
Ruden, S. P., & Pollack, J. B. 1991, ApJ, 375, 740
Shakura, N. I., & Sunyaev, R. A. 1973, A&A, 24, 337
Shu, F. H. 1977, ApJ, 214, 488
Simon, M., Dutrey, A., & Guilloteau, S. 2000, ApJ, 545, 1034
Strom, K. M., Strom, S. E., Edwards, S., Cabrit, S., & Skrutskie, M. F. 1989, AJ, 97, 1451
St-Onge, G., & Bastien, P. 2008, ApJ, 674, 1032
Terquem, C. E. J. M. L. J. 2008, ApJ, 698, 532
Testi, L., Natta, A., Shepherd, D. S., & Wilner, D. 2003, A&A, 403, 323
Toomre, A. 1964, ApJ, 139, 1217
Weidenschilling, S. J. 1977, ApJS, 51, 153
Weingartner, J. C., & Draine, B. T. 2001, ApJ, 563, 842
Watson, D. M., et al. 2004, ApJS, 154, 391
Wichmann, R., Bastian, U., Krautter, J., Jankovics, I., & Rucinski, S. M. 1998, MNRAS, 301, 39
Wilner, D. J., Ho, P. T. P., Kastner, J. H., & Rodríguez, L. F. 2000, ApJ, 534, 101
Wrobel, J. M., & Walker, R. C. 1999, in ASP Conf. Ser. 180, Synthesis Imaging in Radio Astronomy II, A Collection of Lectures from the Sixth NRAO/NMIMT Synthesis Imaging Summer School, ed. G. B. Taylor, C. L. Carilli, & R. A. Perley (San Francisco, CA: ASP), 171
van den Ancker, M. E., de Winter, D., & Tjin A Djie, H. R. E. 1998, A&A, 330, 145
Zubko, V.G., Mennella, V., Colangeli, L., & Bussoletti, E. 1996, MNRAS, 282, 1321